J. Fluid Mech. (1996), *vol.* 307, *pp.* 333–372

A singular perturbation model of fluid dynamics in the vestibular semicircular canal and ampulla

By E. R. DAMIANO† AND R. D. RABBITT
Department of Bioengineering, University of Utah, Salt Lake City, UT 84112, USA

(Received 9 August 1994 and in revised form 22 September 1995)

A matched asymptotic analysis is presented that describes the mechanical response of the vestibular semicircular canals to rotation of the head and includes the fluid–structure interaction which takes place within the enlarged ampullary region of the duct. New theoretical results detail the velocity field in a fluid boundary layer surrounding the cupula. The governing equations were linearized for small perturbations in fluid displacement from the prescribed motion of the head and reduced asymptotically by exploiting the slender geometry of the duct. The results include the pressure drop around the three-dimensional endolymphatic duct and through the transitional boundary layers within the ampulla. Results implicitly include the deflected shape of the cupular partition and provide an expression for the dynamic boundary condition acting on the two surfaces of the cupula. In this sense, the analysis reduces the three-dimensional fluid dynamics of the endolymph to a relatively simple boundary condition acting on the surfaces of the cupula. For illustrative purposes we present specific results modelling the cupula as a simple viscoelastic membrane. New results show that the multi-dimensional fluid dynamics within the enlarged ampulla has a significant influence on the pointwise deflection of the cupula near the crista. The spatially averaged displacement of the cupula is shown to agree with previous macromechanical descriptions of endolymph flow and pressure that ignore the fluid–structure interaction at the cupula. As an example, the model is applied to the geometry of the horizontal semicircular canal of the toadfish, *Opsanus tau*, and results for the deflection of the cupula are compared to individual semicircular canal afferent responses previously reported by Boyle & Highstein (1990). The cupular-shear-angle gain, defined by the angular slope of the cupula at the crista divided by the angular velocity of the head, is relatively constant at frequencies from 0.01 Hz up to 1 Hz. Over this same range, the phase of the cupular shear angle aligns with the angular velocity of the head. Near 10 Hz, the shear-angle gain increases slightly and the phase shows a lead of as much a 30°. Results are sensitive to the cupular stiffness and viscosity. Comparing results to the afferent responses represented within the VIIIth nerve provides additional theoretical evidence that the macromechanical displacement of the cupula accounts for the behaviour of only a subset of afferent fibres.

1. Introduction

The primary function of the vestibular semicircular canals is to transduce angular motion of the head into neural signals that are sent to the brain. Afferent signals orig-

† Current address: Department of Biomedical Engineering, University of Virginia, Charlottesville, VA 22908, USA.

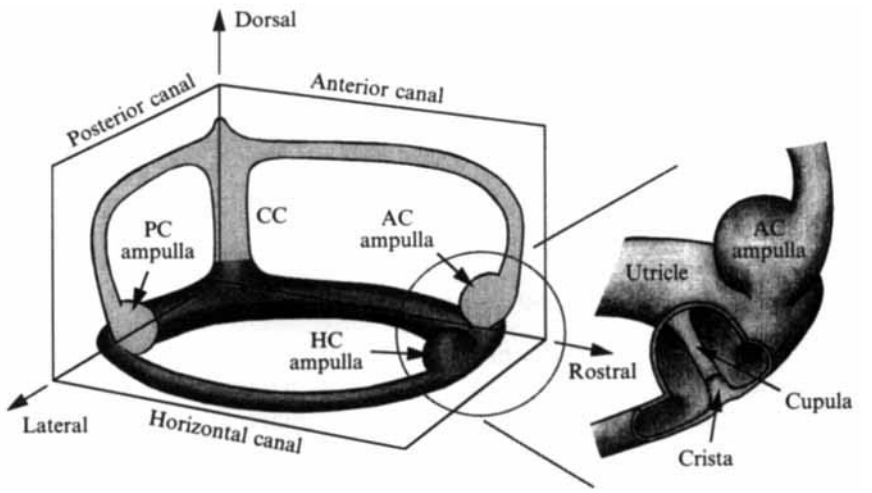

FIGURE 1. Schematic showing the semicircular-canal triad in the toadfish. Salient anatomical features have been indicated. Notice that each duct contains a long-and-slender region with an ampulla at one end while the other end of each duct converges on the enlarged utricle. The anterior and posterior canals (AC and PC, respectively) join at the crus commune (CC) before entering the utricle. The inset details the ampulla of the horizontal canal (HC) showing the cupula-crista system. The sensory epithelium resides on the surface of the crista. The crista is imbedded in the cupula partition which spans an entire cross-section of the ampulla and is impermeable to the endolymphatic fluid.

inating from the canals provide vital inputs that are necessary to maintain dynamic equilibrium and stabilize the image on the retina via the vestibulo-occular, collic, and spinal reflexes. Transduction by the canals is achieved through mechanical activation of the innervated sensory hair cells that reside on the surface of an epithelium. In the present work, the first step in mechanical transduction is described in terms of the unsteady fluid–structure (endolymph–cupula) interaction taking place within the enlarged ampulla. The analysis includes the multi-dimensional ampullary flow and the simpler low-Stokes-number flow in the long-and-slender portion of the duct. A matched asymptotic expansion is utilized to couple the fluid mechanics in the long-and-slender region of the duct to a boundary layer, or transitional flow, in the vicinity of the cupula. The resulting model provides an expression for the transcupular differential pressure which includes the mass and viscous effects of the unsteady flow in the long-and-slender region of the duct as well as the additional dynamics introduced by the three-dimensional unsteady fluid flow in the ampulla. The analysis is applied to the three-dimensional geometry of the toadfish horizontal semicircular canal (see figure 1). Results address the extent to which the fluid dynamics may account for spatial diversity in mechanical activation of sensory hair cells.

The fundamental morpho-physiology of the semicircular canals was first described in the late 19th century by Crum-Brown (1874), Ewald (1887), and Mach (1875). This early work identified the semicircular canals as the source of angular motion sensation and provided a qualitative description of the biomechanics responsible for transduction. Transduction originates with angular acceleration of the head which induces endolymphatic pressure and flow within the fluid-filled semicircular canals. This flow induces deformation of the cupula and deflections of the imbedded stereocilia hair-cell bundles. Deflections of the stereocilia in turn give rise to transduction currents through gating of displacement-sensitive ion channels (Hudspeth 1983; Corey

& Hudspeth 1979, 1983; Hudspeth & Jacobs 1979). The transduction current modulates the receptor potential of hair cells which leads to modulation of the intensity of neurotransmitter vesicle binding and release. Excitatory post-synaptic potentials induced by the neurotransmitter summate to modulate spike initiation in afferents. The response of individual afferent fibres within the VIIIth nerve reflecting this cascade of events has been measured in numerous species (Goldberg & Fernández 1971; Fernández & Goldberg 1971; Blanks, Estes & Markham 1975; Landolt & Correia 1980; Boyle & Highstein 1990; Hartmann & Klinke 1980; Landolt & Correia 1980). Given the vast differences in the species studied, ranging from fish to primates, the response of the nerve is surprisingly uniform. Common features of the response may reflect the morpho-physiological invariance of this phylogenetically old sensory system (Igarashi 1966; Wersäll & Bagger-Sjöbäck 1974; Curthoys & Oman 1987). The three-dimensional fluid-filled toroidal geometry, the enlarged ampulla, and the cupular partition are perhaps the most striking gross morphological inter-species similarities. It is precisely this morphology that is responsible for the macromechanical response of the semicircular canals and the resulting activation of hair-cell mechano-transducers, and it is this morphology that is the subject of the present fluid-dynamical analysis.

The first mathematical description of semicircular canal macromechanics is credited to Steinhausen (1933) who formulated the classical 'torsion-pendulum' model. This analogy views the loop of endolymph as providing rotational inertia, the cupula as providing restoring stiffness, and the viscosity of the endolymph as providing viscous drag. The result is a second-order differential equation for the angular deflection of the pendulum (i.e. the deflection of the cupula) that is forced by the angular acceleration of the head. Since the hair-cell stereocilia are imbedded in the cupula, the deflection of the cupula is typically assumed to be the macromechanical stimulus driving gating of the transduction channels. The torsion-pendulum model is essentially a band-pass filter relating the displacement of the cupula to the angular velocity of the head. Commonly, parameters appearing in the model are related to the geometry and physical properties of the endolymph by assuming steady Poiseuille flow in a uniform toroid acting to deflect a piston at the position of the cupula (Groen 1949, 1957; Van Buskirk 1987; Van Buskirk & Grant 1973; Van Buskirk, Watts & Liu 1976). Analysis of the fluid dynamics was extended to include the non-uniform geometry of the canal by Oman, Marcus & Curthoys (1987) and Rabbitt & Damiano† (1992) using two different modelling techniques but arriving at essentially the same mathematical results. They show that the effective mass loading of the endolymph on the cupula is proportional to the average of the inverse of the local cross-sectional area of the duct. Similarly, the effective viscous loading is proportional to the average of the inverse of the square of the local cross-sectional area of the duct. In addition, Van Buskirk *et al.* (1976) and Rabbitt & Damiano (1992) provide expressions for the velocity distribution in the long-and-slender part of the duct, valid in regions away from the cupula, that locally determine the amplitude and phase of the endolymphatic drag force relative to the flow rate.

Although the more recent models go well beyond Steinhausen's original torsion-pendulum one, all of the previous models agree that the average macromechanical response of the semicircular canal is qualitatively similar to the prediction of the classical model (i.e. essentially a two-time constant band-pass filter). The response of afferent nerves however shows phase and gain enhancements at high physiological

† Figures 5 and 6 reported by Rabbitt & Damiano (1992) are incorrect owing to an error in the original computer implementation. The correct numerical results are provided by Damiano (1993). The reader should refer to the Corrigendum at the end of this volume.

frequencies over and above the gross displacement of the cupula predicted by these mechanical models (Goldberg & Fernández 1971; Fernández & Goldberg 1971; Boyle & Highstein 1990). This may be due to processing interposed between the mechanics and the neural response (i.e. hair-cell and afferent complexes) and/or it may be due to deficiencies in the theoretical mechanical models. Direct measurements of the cupular displacement during physiological stimulation have the potential to resolve this question but such data have not been reported and remain an experimental challenge to obtain. In order to address this question using a mathematical model it is necessary to include the local deflection of the cupula that underlies the mechanical stimuli activating sensory hair cells. Results of the present work show that the deflected shape of the cupula is highly sensitive to cross-sectional endolymph flow near the surface of the cupula – an effect ignored by all previous work.

In the present work we extend analysis of the fluid mechanics to encompass the entire physiological frequency range by including the influence of the multi-dimensional endolymph–cupula interaction. Although unsteady effects are relatively small in the long-and-slender region of the duct, inertia plays a significant role in the enlarged ampullary region and thereby influences the endolymph–cupula interaction. The importance of unsteady flow is evidenced by the relatively large ampullary Stokes number of approximately 6 at 1 Hz. This corresponds to the middle physiological frequency range and continues to increase with increasing frequency.

The endolymphatic flow field is determined by solving a singular perturbation problem describing the fluid dynamics throughout a single semicircular canal. What makes the equations singular are derivatives along the length of the duct which are asymptotically small everywhere except within the ampulla. To account for this, a boundary layer is included in the neighbourhood of the cupula. In this boundary-layer region, the flow is complicated by the interaction with the cupula and the enlarged cross-sectional area of the canal. We use the analysis of the flow in the long-and-slender part of the distorted toroid by Rabbitt & Damiano (1992) to describe the 'outer-region' of the asymptotic solution. A new analysis is presented to describe the flow in the ampullary region. Between the two regions the solutions are asymptotically matched (refer to Kevorkian & Cole 1981 and Van Dyke 1975 for a discussion of these methods). A principal result of the work is a new expression that compresses the entire fluid-dynamical problem into a boundary condition acting on the surfaces of the cupula. The result relates the pressure differential acting across the cupula to the acceleration of the head and to the motion of the cupula itself. It is shown in § 3 that the pressure, Δp^*, acting transversely across the cupula is given by

$$\Delta p^* = \Delta p_i^* - \Delta p_m^* - \Delta p_v^* - \Delta p_b^*, \tag{1.1}$$

where

$$\Delta p_i^*(t^*) = -\rho \int_0^l \frac{\mathrm{d}^2 \boldsymbol{\Omega}^*}{\mathrm{d}t^{*2}} \times \boldsymbol{R}^* \cdot \mathbf{d}\boldsymbol{s}_\circ^*, \tag{1.2}$$

$$\Delta p_m^*(t^*) = \rho \int_0^l \frac{\boldsymbol{n} \cdot \mathbf{d}\boldsymbol{s}_\circ^*}{A^*} \iint_{A_p^*} \frac{\partial^2 w^*}{\partial t^{*2}} \mathrm{d}A^*, \tag{1.3}$$

$$\Delta p_v^*(t^*) = \mu \int_0^l \frac{\lambda}{A^{*2}} \boldsymbol{n} \cdot \mathbf{d}\boldsymbol{s}_\circ^* \iint_{A_p^*} \frac{\partial w^*}{\partial t^*} \mathrm{d}A^*, \tag{1.4}$$

$$\Delta p_b^*(r^*, t^*) = \mu \sum_{n=1}^{\infty} \left(\frac{\beta_n^2}{a_p^{*2}} + \mathrm{i} \frac{\omega}{\nu} \right)^{1/2} \frac{\left\langle \frac{\partial w^*}{\partial t^*}, J_0(\beta_n r^*/a_p^*) \right\rangle}{\langle J_0(\beta_n r^*/a_p^*), J_0(\beta_n r^*/a_p^*) \rangle} J_0(\beta_n r^*/a_p^*). \tag{1.5}$$

Here, the displacement field of the cupula is given by $w^* = w^*(r^*, t^*)$ where r^* is the radial coordinate in the cross-section of the canal and t^* is time. The density, dynamic viscosity, and kinematic viscosity of the endolymphatic fluid are respectively given by ρ, μ, and $\nu = \mu/\rho$. The local cross-sectional area of the canal is given by $A^* = A^*(s^*)$ while $\boldsymbol{R}^* = \boldsymbol{R}^*(s^*)$ defines the position vector from the axis of rotation to the centre of a cross-section at s^* where s^* is the curvilinear axial coordinate along the canal of total length l. The unit tangent vector to the (circular) curvilinear path defined by s^* is given by $\boldsymbol{n}$ while the differential tangent vector to the curvilinear path described by the centreline of the canal is given by $\mathbf{d}\boldsymbol{s}_c^*$. The region of integration, $A_p^* = \pi a_p^{*2}$, corresponds to the area occupied by the surface of the cupula partition. The angular displacement vector of the canal is given by $\boldsymbol{\Omega}^*$ and its rotational frequency is given by ω. The eigenvalues, β_n, are the zeros of the zeroth-order Bessel function of the first kind, J_0.

This relatively simple result is written in dimensional form (symbols which carry an asterisk indicate dimensional variables) and includes the three-dimensional morphology of the endolymphatic duct, the unsteady fluid dynamics throughout the toroid, and the fluid–structure interaction at the cupula. It is intended for use with multi-dimensional biomechanical models of the cupula and sensory epithelium. The pressure implicitly includes the spatio-temporal displacement of the cupula and is valid regardless of the specific cupular model employed. The first term, given by (1.2), is the inertial forcing caused by the angular acceleration of the head. The second term, given by (1.3), is the effective mass loading of the entire loop of endolymph acting on the cupula. Similarly, the third term, given by (1.4), represents the effective viscous loading of the entire loop of endolymph in terms of the average velocity of the cupula. The fourth term, given by (1.5), accounts for the local mass and viscous effects in the neighbourhood of the cupula arising from the multi-dimensional fluid dynamics occurring within the ampulla. The first two terms above, given by Δp_i^* and Δp_m^*, were first obtained by Oman *et al.* (1987) using an alternative method. The third term, given by Δp_v^*, differs from the model of Oman *et al.* (1987) owing to the appearance of the parameter λ which provides the frequency dependence of the magnitude and phase of the viscous drag in the long-and-slender portion of the duct. The new result of the present work is the fourth term given above by Δp_b^*. The analysis presented herein is concerned solely with the derivation of the cupular boundary condition given by (1.1). As an illustrative example, the boundary condition is applied to the toadfish horizontal semicircular canal treating the cupula as a linear viscoelastic membrane (Rabbitt, Boyle & Highstein 1994, 1995*a*; Damiano 1993).

We begin the analysis with the derivation of the flow in the 'outer-region' (§ 2) which is valid far from the cupula. This is asymptotically matched to a 'boundary layer' (§ 3) on both sides of the cupula within the ampulla. Analysis of the fluid mechanics is followed by a numerical example that illustrates the significance of the boundary layer. For this we formulate a simple two-dimensional model of the cupula (§ 4) and solve the coupled equations numerically (§ 5).

2. The outer region

We follow the approach of Rabbitt & Damiano (1992) to describe flow in the long-and-slender region of the duct and the utricle. New results match this 'outer-region' solution to a 'boundary-layer' model of the endolymph–cupula interaction within the ampulla. We begin with a brief description of the outer expansion that is necessary in order to proceed with the boundary-layer analysis in § 3.

The endolymph is modelled as an incompressible Newtonian fluid governed by the Navier–Stokes equations,

$$\frac{\partial \boldsymbol{v}^*}{\partial t^*} + (\boldsymbol{v}^* \cdot \nabla^*)\boldsymbol{v}^* = -\frac{1}{\rho}\nabla^* p^* + \nu \nabla^{*2}\boldsymbol{v}^*, \tag{2.1}$$

where $\boldsymbol{v}^*$ is the dimensional fluid velocity vector, p^* is the dimensional fluid pressure, and the parameters ρ and ν are the endolymphatic density and kinematic viscosity, respectively. Quantities carrying an asterisk refer to dimensional variables while all other variables are non-dimensional. In addition to these equations, the divergence of velocity vanishes everywhere consistent with the assumption of endolymph incompressibility.

The equations governing the fluid are cast in terms of the locally orthogonal toroidal coordinate system (r^*, φ, s^*) defined by the transformation from the Cartesian coordinates (x^*, y^*, z^*) given by

$$x^* = (r^* \cos\varphi + R_0)\cos(s^*/R_0), \tag{2.2}$$

$$y^* = (r^* \cos\varphi + R_0)\sin(s^*/R_0), \tag{2.3}$$

$$z^* = r^* \sin\varphi. \tag{2.4}$$

Here r^* and φ are the polar cross-sectional coordinates and s^* is the axial coordinate of a toroid of constant radius of curvature $1/R_0$. Figure 2 shows orthographic projections of the three-dimensional geometry which is used to model the horizontal semicircular canal of the oyster toadfish, *Opsanus tau*. The Navier–Stokes equations are expressed in these toroidal coordinates and non-dimensionalized. The dimensionless variables are defined as follows:

$$\boldsymbol{v} = \boldsymbol{v}^*/U \;; \quad p = \varepsilon p^*/\tfrac{1}{2}\rho U^2, \tag{2.5}$$

and

$$r = r^*/a_0 \;; \quad s = s^*/l \;; \quad t = \omega t^*, \tag{2.6}$$

where $l = 2\pi R_0$ is the length of the toroid, U is the characteristic velocity, ω is the characteristic frequency, and a_0 is the characteristic cross-sectional radius of the duct (numerical values for the parameter sets used in this analysis are listed in table 1 for the toadfish canal system). The dimensionless equations of motion are expanded in powers of the slenderness ratio, $\varepsilon = a_0/l$. They are given by Rabbitt & Damiano (1992) to $O(\varepsilon)$ as follows:

$$\frac{St}{Re}\frac{\partial v_s}{\partial t} + \boldsymbol{v}_c \cdot \nabla_c v_s - \frac{1}{Re}\nabla_c^2 v_s + \frac{1}{2}\frac{\partial p}{\partial s} + O(\varepsilon) = 0, \tag{2.7}$$

$$\frac{\partial p}{\partial r} + O(\varepsilon) = 0 \;; \quad \frac{1}{r}\frac{\partial p}{\partial \varphi} + O(\varepsilon) = 0, \tag{2.8}$$

where $St = a_0^2\omega/\nu$ and $Re = Ua_0/\nu$ are the Stokes and Reynolds numbers, respectively. Here we mean by the subscript c that the differential operator or vector is to apply to the cross-sectional coordinates only. Thus, $\boldsymbol{v}_c$ is the cross-sectional velocity vector given by $v_r\boldsymbol{e}_r + v_\varphi \boldsymbol{e}_\varphi$ where $\boldsymbol{e}_r$ and $\boldsymbol{e}_\varphi$ are the unit base vectors in the cross-section of the toroidal coordinate system. The gradient and Laplacian over the cross-section are defined in the usual way such that

$$\nabla_c = \frac{\partial}{\partial r}\boldsymbol{e}_r + \frac{1}{r}\frac{\partial}{\partial \varphi}\boldsymbol{e}_\varphi \quad \text{and} \quad \nabla_c^2 = \frac{\partial^2}{\partial r^2} + \frac{1}{r}\frac{\partial}{\partial r} + \frac{1}{r^2}\frac{\partial^2}{\partial \varphi^2}.$$

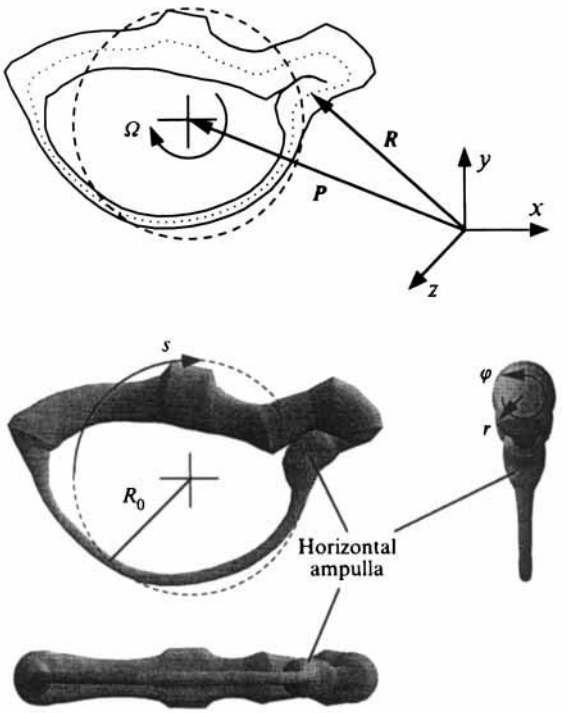

FIGURE 2. Orthographic projections of the geometry used to model the horizontal semicircular canal of the toadfish, *Opsanus tau*. The gross geometry was obtained from a tracing (top) of a digitized micrograph showing the outline of the horizontal canal of an adult toadfish perpendicular to the plane of the duct. In constructing the orthographic projections for the three-dimensional model geometry, individual cross-sections were assumed to be circular with their centres falling within a single plane. The actual geometry consists of elliptical cross-sections in which the minor and major axes vary along the length of the canal. The locally orthogonal toroidal coordinates are superimposed on the orthographic projections and the Cartesian coordinate position vectors are shown relative to the canal tracing.

For the special case of sinusoidal rotation of the head, a solution is sought in the form of an asymptotic expansion of the velocity and pressure. Furthermore, the cross-sectional velocity vector, $\boldsymbol{v}_c$, is taken to be $O(\varepsilon)$ in the long-and-slender outer region but not in the ampulla. For the case of pure rotation then, the dependent variables in the outer region are expanded in the form

$$\boldsymbol{v}_c \sim \varepsilon \boldsymbol{v}_{c_1} + \varepsilon^2 \boldsymbol{v}_{c_2} + \cdots, \tag{2.9}$$

$$v_s \sim v_{s_0} + \varepsilon v_{s_1} + \varepsilon^2 v_{s_2} + \cdots, \tag{2.10}$$

$$p \sim p_0 + \varepsilon p_1 + \varepsilon^2 p_2 + \cdots. \tag{2.11}$$

Substitution into (2.7) and (2.8) provides the leading-order model of momentum conservation in the canals. Accordingly, by (2.8), the pressure, p_0, is a function only of the axial coordinate, s, and time, t. Furthermore, in light of the asymptotic expansions above, the s-momentum equation, given by (2.7), is linear in v_{s_0}.

Applying the no-slip condition, the velocities of the fluid and the duct wall must match at their interface. To leading order, in the case of pure rotation, the boundary condition is given by $v_{s_0}|_w = R(s)\dot{\Omega}(t)$ where the subscript w refers to the duct wall, $R(s)$ is the normalized distance from the centroid of the duct to the centre of a given

Parameter or Property	Value
a_0, characteristic cross-sectional radius of duct	0.019 cm
l, length of duct	2.75 cm
$\varepsilon = a_0/l$, slenderness ratio	0.007
$1/R_0 = 2\pi/l$, characteristic radius of curvature of duct	2.29 cm^{-1}
$R_p^* = \lvert \boldsymbol{R}_p^* - \boldsymbol{P}^* \rvert$, distance from canal centroid to centre of cupula	0.4 cm
$a_p^* = a_0 a_p$, cross-sectional radius of cupula	0.09 cm
$A_p^* = \pi a_p^{*2}$, cross-sectional area of ampulla at cupula	0.025 cm^2
ρ, endolymphatic fluid density	1.0 g cm^{-3}
$\nu = \mu/\rho$, endolymphatic fluid kinematic viscosity	0.0085 cm^2 s^{-1}
ρ_p, cupula partition density	1.0 g cm^{-3}
$\nu_p = \mu_p/\rho_p$, cupula partition kinematic viscosity	0.0085 – 29.0 cm^2 s^{-1}
T, cupula partition membrane stiffness	0.0035 – 0.35 dyn cm^{-1}
h, cupula partition thickness	0.05 cm
$\int_0^1 \frac{\ddot{\Omega}}{\ddot{\Omega}} \times \boldsymbol{R} \cdot \mathbf{ds}_\circ$, inertial forcing coefficient	1.04 $cm^2 \times 2\pi/l^2$
$\int_0^1 \frac{\boldsymbol{n} \cdot \mathbf{ds}_\circ}{A}$, mass coefficient	1.11 $\times 10^3$ $cm^{-1} \times a_0^2/l$
Re $\left(\int_0^1 \frac{\lambda}{A^2} \boldsymbol{n} \cdot \mathbf{ds}_\circ \right)$, real part of viscous coefficient	3.30 $\times 10^7$ $cm^{-3} \times a_0^4/l$ (at 1 Hz)
Im $\left(\int_0^1 \frac{\lambda}{A^2} \boldsymbol{n} \cdot \mathbf{ds}_\circ \right)$, imaginary part of viscous coefficient	3.15 $\times 10^5$ $cm^{-3} \times a_0^4/l$ (at 1 Hz)

TABLE 1. Physical parameters and properties of the canal, endolymphatic fluid, and cupula partition in the toadfish, *Opsanus tau*. The dimensionless coefficients of terms appearing in the transcupular differential pressure given by (2.14) are also listed for the toadfish geometry.

cross-section at s, and $\dot{\Omega}(t)$ is the non-dimensional angular velocity of the duct wall (where the dot indicates an ordinary time derivative).

The resulting model is transformed into an inhomogeneous equation with homogeneous boundary conditions by introducing the variable $u = v_s - v_s|_w$ which represents the relative velocity of the endolymph in the axial direction with respect to the duct wall. The resulting $O(1)$ equation and boundary condition are given by

$$\frac{St}{Re}\frac{\partial u_0}{\partial t} - \frac{1}{Re}\nabla_c^2 u_0 + \frac{1}{2}\frac{\partial p_0}{\partial s} = -\frac{St}{Re} R \ddot{\Omega}, \tag{2.12}$$

and

$$u_0|_w = 0. \tag{2.13}$$

The contribution of the outer region to the pressure differential acting across the ampulla is determined from the endolymphatic fluid dynamics. Following the procedure of Rabbitt & Damiano (1992), (2.12) is integrated over the cross-section, $A(s)$, and then over the length of the duct to obtain the pressure differential, Δp_0. Applying the divergence theorem, and making use of integral continuity for an incompressible fluid, provide the zero-order pressure differential in terms of the displacement of the cupula and the viscous interaction between the endolymph and the duct wall. A viscous-shear-stress factor, λ, is defined which accounts for the

influence of the shape of the cross-sectional velocity profile on the viscous drag at the wall. Solving for the endolymphatic velocity field from (2.12), the pressure differential is determined implicitly in terms of the leading-order displacement, w_0, of the cupula partition. This is given by

$$\Delta p_0 = -2\frac{St}{Re}\left\{\int_0^1 \ddot{\boldsymbol{\Omega}} \times \boldsymbol{R} \cdot \mathbf{ds}_\circ + \int_0^1 \frac{\boldsymbol{n} \cdot \mathbf{ds}_\circ}{A} \iint_{A_p} \frac{\partial^2 w_0}{\partial t^2} \mathrm{d}A\right\} - \frac{2}{Re}\int_0^1 \frac{\lambda}{A^2} \boldsymbol{n} \cdot \mathbf{ds}_\circ \iint_{A_p} \frac{\partial w_0}{\partial t} \mathrm{d}A, \tag{2.14}$$

where A_p is the region of integration corresponding to the dimensionless area of the cupula partition, $\boldsymbol{R}$ is the dimensionless position vector from the axis of rotation to the centre of a given cross-section at s, $\mathbf{ds}_\circ$ is the differential tangent vector to the curvilinear path along the centreline of the duct, and $\boldsymbol{n}$ is the unit tangent vector to the axial curvilinear coordinate curve. The dimensionless differential pressure given above applies only to the outer region and accounts for the first three terms on the right-hand side of (1.1). The derivation of the remaining term is provided in § 3.

The viscous-shear-stress factor, λ, appearing in the third term of (2.14), is a complex-valued frequency-dependent function of s and is given by

$$\lambda \equiv -\pi \int_{\partial A} \frac{\partial u_0}{\partial r} \mathrm{d}\sigma \Big/ \iint_A u_0 \, \mathrm{d}A. \tag{2.15}$$

The parameter λ determines the magnitude and phase of the viscous shear stress at the wall relative to the flow rate. At low frequencies, where the velocity profile is approximately a Poiseuille flow, the viscous-shear-stress factor is 8π for a circular tube. Pedley, Schroter & Sudlow (1971) describe an analogous parameter (referred to as Z rather than λ) in terms of the rate of energy dissipation for various flows (e.g. entry flow into a tube, turbulent flow in a tube, and tube flow near branches) relative to the energy dissipation rate which accompanies fully developed Poiseuille flow in a straight cylindrical tube.

For the case of axisymmetric flow in the long-and-slender portion of the duct, the endolymphatic velocity profile is given by the Fourier–Bessel series

$$u_0(r, s, t) = -g(s)\, \mathrm{e}^{\mathrm{i}t} \sum_{n=1}^{\infty} \left\{\frac{\langle 1, J_{0_n}\rangle}{k_n^2(s)\langle J_{0_n}, J_{0_n}\rangle}\right\} J_0(\alpha_n(s) r), \tag{2.16}$$

where $k_n^2(s) = \alpha_n^2(s) + \mathrm{i}\, St$, $\alpha_n^2(s) = \beta_n^2/a^2(s)$, and the eigenvalues, β_n, are the zeros of the zeroth-order Bessel function, J_0. Unless otherwise indicated, the notation J_{0_n} is meant to represent $J_0(\alpha_n r)$. The inner products above are defined with respect to the cross-section such that

$$\langle f, g\rangle = \iint_A fg \, \mathrm{d}A. \tag{2.17}$$

The amplitude function, $g(s)$, is determined by substituting (2.16) into the integral form of continuity given by

$$\frac{\partial}{\partial s} \iint_A u_0 \, \mathrm{d}A = 0. \tag{2.18}$$

With the unsteady velocity profile determined from (2.16), the viscous-shear-stress factor, given by (2.15), may be readily ascertained. Figure 3 shows the real and imaginary parts of λ plotted as a function of the local Stokes number. The curves are

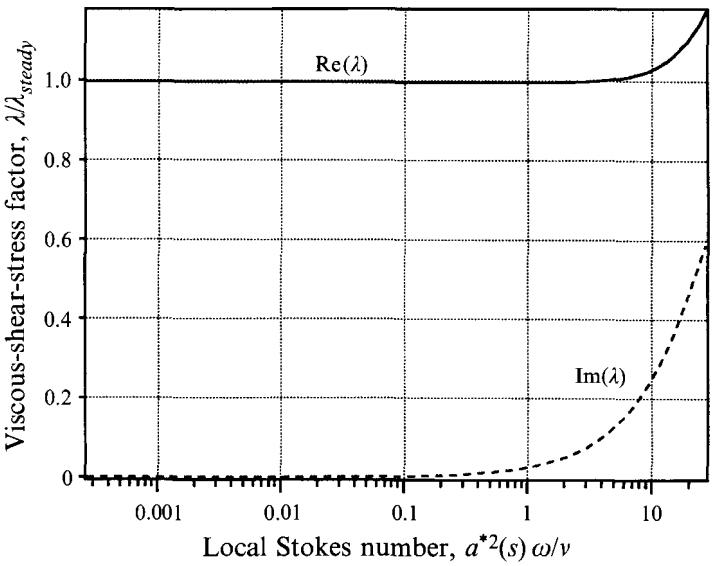

FIGURE 3. The frequency dependence of the real and imaginary parts of the viscous-shear-stress factor, λ, is shown for the case of sinusoidal flow in a tube of circular cross-section. Results are computed using (2.15) and are shown as a function of the local Stokes number, $(St)_s = a(s)St = a^{*2}(s)\omega/\nu$. Notice that below a Stokes number of 1, the unsteady effects are unimportant. As a result, the velocity profile in the long-and-slender region of the duct is essentially Poiseuille over the entire physiological frequency range but involves unsteady phase and viscous drag effects in the utricle and in the ampulla. In the present model, the unsteady flow in the utricle is included as part of the outer-region solution and coupling of the unsteady flow to the cupula is included in the ampullary boundary layer.

normalized with respect to 8π which corresponds to the steady value for Poiseuille flow in a circular duct. For the toadfish, in the long-and-slender portion of the duct where the cross-sectional radius is approximately 0.019 cm, a Stokes number of 1 corresponds to a frequency of 3.75 Hz, whereas in the ampulla the same Stokes number corresponds to a frequency of approximately 0.17 Hz. Thus, the unsteady effects play a significant role in influencing the shape of the velocity profile in the ampulla and utricle at upper physiological frequencies but are of little consequence in the long-and-slender portion of the duct.

3. The boundary layer

The perturbation method which was applied in the previous section to the outer region exploited the slenderness ratio of the toroidal duct allowing us to order the relative size of the derivatives appearing in the Navier–Stokes equations. We found the cross-sectional derivatives of the fluid velocities to be much larger than their counterparts in the axial direction. This is a consequence of the slender geometry. However, this asymptotic ordering is not uniformly valid over the entire flow field. In particular, within a relatively small layer surrounding the cupula, the rate of change of the velocity profile with respect to the axial direction is quite large, particularly at high physiological frequencies. In this ampullary 'boundary-layer' region, the magnitude of the axial derivatives approaches those in the cross-section so the outer-region solution does not apply. Physically this corresponds to a transition flow that matches the fluid moving with the deflected shape of the cupula to the

velocity profile in regions far from the cupula. At low frequencies the influence of the ampullary boundary layer is negligible. However, when the forcing frequency is large (above 1 Hz) the multi-dimensionality becomes more pronounced and the local entrainment of endolymph by the cupula plays an important role. To quantify this, we match the fluid dynamics in the outer region to a boundary layer acting within the ampulla.

The boundary-layer term, Δp_b^*, is found by solving the three-dimensional Navier–Stokes equations within a layer on each side of the cupula and requiring that the solution asymptotically match the outer-region solution far from the cupula. We begin by considering the non-dimensional momentum equation in the s-direction expanded in powers of the slenderness ratio, ε, given by

$$\frac{St}{Re}\frac{\partial v_s}{\partial t} + \boldsymbol{v}_c \cdot \nabla_c v_s - \frac{1}{Re}\nabla_c^2 v_s + \frac{1}{2}\frac{\partial p}{\partial s} + \left\{ v_r v_s \cos\varphi - v_\varphi v_s \sin\varphi + \frac{v_s}{2\pi}\frac{\partial v_s}{\partial s} \right.$$
$$\left. - \frac{1}{Re}\left(\cos\varphi \frac{\partial v_s}{\partial r} - \frac{\sin\varphi}{r}\frac{\partial v_s}{\partial \varphi}\right) - r\cos\varphi \frac{1}{2}\frac{\partial p}{\partial s} \right\} 2\pi\varepsilon$$
$$+ \left\{ r\cos\varphi \left(\sin\varphi\, v_\varphi v_s - \cos\varphi\, v_r v_s - \frac{v_s}{2\pi}\frac{\partial v_s}{\partial s} \right) \right.$$
$$- \frac{1}{Re}\left(\frac{\cos\varphi}{\pi}\frac{\partial v_r}{\partial s} - \frac{\sin\varphi}{\pi}\frac{\partial v_\varphi}{\partial s} - v_s + \frac{1}{4\pi^2}\frac{\partial^2 v_s}{\partial s^2} + r\cos\varphi\sin\varphi\frac{\partial v_s}{\partial \varphi} - r\cos^2\varphi\frac{\partial v_s}{\partial r} \right)$$
$$\left. + r^2\cos^2\varphi \frac{1}{2}\frac{\partial p}{\partial s} \right\} 4\pi^2\varepsilon^2 + O(\varepsilon^3) = 0. \tag{3.1}$$

We define a boundary-layer coordinate, $\tilde{s}$, corresponding to a stretching of the s-coordinate in which the stretching factor depends on ε according to $\tilde{s} = (s - s_p)/\varepsilon^\alpha$ where α is positive and s_p is the s-coordinate location of the cupula partition. On one side of the cupula $s_p = 0$ and $\tilde{s} \geqslant 0$, on the other $s_p = 1$ and $\tilde{s} \leqslant 0$. In the boundary layer the cross-sectional velocity components may be of the same order of magnitude as the axial component. We define the velocity vector there to be given by $\tilde{\boldsymbol{v}} = \tilde{\boldsymbol{v}}(r, \varphi, \tilde{s}, t) = \tilde{\boldsymbol{v}}_c + \tilde{v}_s \boldsymbol{e}_s$ and assume an asymptotic expansion in the boundary layer given by

$$\tilde{\boldsymbol{v}}_c(r, \varphi, \tilde{s}, t) \sim \tilde{\boldsymbol{v}}_{c_0} + \varepsilon\tilde{\boldsymbol{v}}_{c_1} + \cdots, \tag{3.2}$$
$$\tilde{v}_s(r, \varphi, \tilde{s}, t) \sim \tilde{v}_{s_0} + \varepsilon\tilde{v}_{s_1} + \varepsilon^2\tilde{v}_{s_2} + \cdots, \tag{3.3}$$
$$\tilde{p}(r, \varphi, \tilde{s}, t) \sim \tilde{p}_0(\tilde{s}, t) + \varepsilon\tilde{p}_1 + \varepsilon^2\tilde{p}_2 + \cdots. \tag{3.4}$$

Here, the multi-dimensional pressure distribution in the boundary layer is superimposed on the cross-sectionally averaged $O(1)$ pressure, $p_0(s, t)$, found in the outer solution. Using these expansions in the momentum equation given by (3.1) and expressing it in terms of the boundary-layer coordinate, $\tilde{s}$, the conservation of momentum in the axial direction in the boundary layer is given by

$$\frac{St}{Re}\frac{\partial \tilde{v}_{s_0}}{\partial t} + \tilde{\boldsymbol{v}}_{c_0} \cdot \nabla_c \tilde{v}_{s_0} + \varepsilon^{1-\alpha}\tilde{v}_{s_0}\frac{\partial \tilde{v}_{s_0}}{\partial \tilde{s}} - \frac{1}{Re}\left(\nabla_c^2 \tilde{v}_{s_0} + \varepsilon^{2-2\alpha}\frac{\partial^2 \tilde{v}_{s_0}}{\partial \tilde{s}^2} \right)$$
$$+ \frac{\varepsilon^{-\alpha}}{2}\frac{\partial \tilde{p}_0}{\partial \tilde{s}} + \varepsilon^{1-\alpha}\left(\frac{1}{2}\frac{\partial \tilde{p}_1}{\partial \tilde{s}} - \pi r\cos\varphi\frac{\partial \tilde{p}_0}{\partial \tilde{s}} \right) + O(\varepsilon^{2-\alpha}) = 0. \tag{3.5}$$

Balancing powers of ε, the distinguished limit (Kevorkian & Cole 1981) is $\alpha = 1$ and we obtain the $O(1/\varepsilon)$ problem in the boundary layer as being $\partial \tilde{p}_0/\partial \tilde{s} = 0$ or $\tilde{p}_0 = \tilde{p}_0(t)$ only. Thus at any instant in time, p_0 is constant throughout the boundary layers on both sides of the cupula and equal to its value on either side of the cupula at $s = s_p$ (which in general is different on one side than on the other). With this result, the $O(1)$ equation in the boundary layer reduces to

$$\frac{St}{Re}\frac{\partial \tilde{v}_{s_0}}{\partial t} + \tilde{\boldsymbol{v}}_{c_0} \cdot \nabla_c \tilde{v}_{s_0} + \tilde{v}_{s_0}\frac{\partial \tilde{v}_{s_0}}{\partial \tilde{s}} - \frac{1}{Re}\left(\nabla_c^2 \tilde{v}_{s_0} + \frac{\partial^2 \tilde{v}_{s_0}}{\partial \tilde{s}^2}\right) + \frac{1}{2}\frac{\partial \tilde{p}_1}{\partial \tilde{s}} = 0. \tag{3.6}$$

Since $\tilde{s} = s/\varepsilon$, the $O(1)$ momentum equations governing the cross-sectional velocity vector, $\tilde{\boldsymbol{v}}_c$, in the boundary layer become

$$\frac{St}{Re}\frac{\partial \tilde{v}_{r_0}}{\partial t} + \tilde{\boldsymbol{v}}_{c_0} \cdot \nabla_c \tilde{v}_{r_0} - \frac{\tilde{v}_{\varphi_0}^2}{r} + \tilde{v}_{s_0}\frac{\partial \tilde{v}_{r_0}}{\partial \tilde{s}} - \frac{1}{Re}\left(\nabla_c^2 \tilde{v}_{r_0} - \frac{\tilde{v}_{r_0}}{r^2} - \frac{2}{r^2}\frac{\partial \tilde{v}_{\varphi_0}}{\partial \varphi} + \frac{\partial^2 \tilde{v}_{r_0}}{\partial \tilde{s}^2}\right) + \frac{1}{2}\frac{\partial \tilde{p}_1}{\partial r} = 0, \tag{3.7}$$

and

$$\frac{St}{Re}\frac{\partial \tilde{v}_{\varphi_0}}{\partial t} + \tilde{\boldsymbol{v}}_{c_0} \cdot \nabla_c \tilde{v}_{\varphi_0} + \frac{\tilde{v}_{r_0}\tilde{v}_{\varphi_0}}{r} + \tilde{v}_{s_0}\frac{\partial \tilde{v}_{\varphi_0}}{\partial \tilde{s}} - \frac{1}{Re}\left(\nabla_c^2 \tilde{v}_{\varphi_0} - \frac{\tilde{v}_{\varphi_0}}{r^2} + \frac{2}{r^2}\frac{\partial \tilde{v}_{r_0}}{\partial \varphi} + \frac{\partial^2 \tilde{v}_{\varphi_0}}{\partial \tilde{s}^2}\right) + \frac{1}{2r}\frac{\partial \tilde{p}_1}{\partial \varphi} = 0. \tag{3.8}$$

Thus the $O(1)$ equations of motion in the boundary layer reduce to the Navier–Stokes equations expressed in cylindrical coordinates applied to the velocity vector, $\tilde{\boldsymbol{v}}$.

Imposing the no-slip boundary condition, the velocity of the viscous endolymphatic fluid must exactly match that of the rigid impermeable duct wall at their interface. For pure rotation, the $O(1)$ velocity of the duct wall is given by $R(\varepsilon\tilde{s})\,\dot{\Omega}(t)\,\boldsymbol{e}_s$, where $R(\varepsilon\tilde{s})$ is the normalized distance from the centroid of the duct to the centre of a given cross-section at $\tilde{s}$ and $\dot{\Omega}(t)$ is the non-dimensional angular velocity of the duct wall. In the boundary layer, the dimensionless quantity R varies slowly with $\tilde{s}$ and has the expansion $R(\varepsilon\tilde{s}) = R(0) + \varepsilon^2\tilde{s}R'(0) + \cdots$. Thus to a leading-order approximation we take this quantity to be constant and equal to its value at the cupula partition. In the boundary layer then, R is approximated by $R(0) = R_p = R_p^*/R_0$ where R_p^* is the dimensional distance from the centroid of the duct to the centre of the cupula. This effectively neglects the curvature of the canal wall in the boundary-layer region (which is validated in § 6 by numerical evaluation of the cupular boundary-layer thickness). For pure rotation of the duct, the endolymph velocity relative to the duct wall must vanish on the boundary as a result of the no-slip condition and impermeability of the duct wall. Thus, the leading-order boundary condition on the velocity, $\tilde{\boldsymbol{v}}_0$, is given by $\tilde{\boldsymbol{v}}_{c_0}|_w = \boldsymbol{0}$ and $\tilde{v}_{s_0}|_w = R_p\,\dot{\Omega}$, where the subscript w refers to the duct wall.

We transform (3.6) into an inhomogeneous equation with homogeneous boundary conditions by introducing the variable $\tilde{u} = \tilde{v}_s - \tilde{v}_s|_w$ which represents the relative velocity of the endolymph in the axial direction with respect to the duct wall. To leading order, this transformation corresponds to $\tilde{u}_0 = \tilde{v}_{s_0} - R_p\,\dot{\Omega}$. Expressing (3.6) in terms of the variable $\tilde{u}_0$ results in an $O(1)$ equation and boundary condition given by

$$\frac{St}{Re}\frac{\partial \tilde{u}_0}{\partial t} + \tilde{\boldsymbol{v}}_{c_0} \cdot \nabla_c \tilde{u}_0 + (\tilde{u}_0 + R_p\,\dot{\Omega})\frac{\partial \tilde{u}_0}{\partial \tilde{s}} - \frac{1}{Re}\tilde{\nabla}^2 \tilde{u}_0 + \frac{1}{2}\frac{\partial \tilde{p}_1}{\partial \tilde{s}} = -\frac{St}{Re}R_p\,\ddot{\Omega}, \tag{3.9}$$

$$\tilde{u}_0|_w = 0, \tag{3.10}$$

where $\tilde{\nabla}^2$ is the standard Laplacian corresponding to the cylindrical coordinates r, φ, and $\tilde{s}$ given by

$$\tilde{\nabla}^2 = \nabla_c^2 + \frac{\partial^2}{\partial \tilde{s}^2}.$$

Next, we attach a reference frame to the duct wall by defining the Galilean transformation $\bar{s} = \tilde{s} - R_p \Omega Re/St$. Determination of the derivatives with t and $\tilde{s}$ from the chain rule and substitution into (3.9) provide the nonlinear $O(1)$ equation of motion governing the axial velocity component of the fluid in the boundary layer relative to the duct wall and referenced to a coordinate system attached to the duct wall. This is given by

$$\frac{St}{Re}\frac{\partial \tilde{u}_0}{\partial t} + \tilde{\boldsymbol{v}}_{c_0} \cdot \nabla_c \tilde{u}_0 + \tilde{u}_0 \frac{\partial \tilde{u}_0}{\partial \bar{s}} - \frac{1}{Re}\tilde{\nabla}^2 \tilde{u}_0 + \frac{1}{2}\frac{\partial \tilde{p}_1}{\partial \bar{s}} = -\frac{St}{Re} R_p \ddot{\Omega}, \tag{3.11}$$

where the axial derivative in the Laplacian operator is now with respect to $\bar{s}$.

In a similar manner, we apply the same Galilean transformation to the cross-sectional momentum equations and express them in terms of the relative axial velocity component, $\tilde{u}_0$. To leading order then, (3.7) and (3.8) become

$$\frac{St}{Re}\frac{\partial \tilde{v}_{r_0}}{\partial t} + \tilde{\boldsymbol{v}}_{c_0} \cdot \nabla_c \tilde{v}_{r_0} - \frac{\tilde{v}_{\varphi_0}^2}{r} + \tilde{u}_0 \frac{\partial \tilde{v}_{r_0}}{\partial \bar{s}} - \frac{1}{Re}\left(\tilde{\nabla}^2 \tilde{v}_{r_0} - \frac{\tilde{v}_{r_0}}{r^2} - \frac{2}{r^2}\frac{\partial \tilde{v}_{\varphi_0}}{\partial \varphi}\right) + \frac{1}{2}\frac{\partial \tilde{p}_1}{\partial r} = 0, \tag{3.12}$$

$$\frac{St}{Re}\frac{\partial \tilde{v}_{\varphi_0}}{\partial t} + \tilde{\boldsymbol{v}}_{c_0} \cdot \nabla_c \tilde{v}_{\varphi_0} + \frac{\tilde{v}_{r_0}\tilde{v}_{\varphi_0}}{r} + \tilde{u}_0 \frac{\partial \tilde{v}_{\varphi_0}}{\partial \bar{s}} - \frac{1}{Re}\left(\tilde{\nabla}^2 \tilde{v}_{\varphi_0} - \frac{\tilde{v}_{\varphi_0}}{r^2} + \frac{2}{r^2}\frac{\partial \tilde{v}_{r_0}}{\partial \varphi}\right) + \frac{1}{2r}\frac{\partial \tilde{p}_1}{\partial \varphi} = 0, \tag{3.13}$$

with the homogeneous boundary condition, $\tilde{\boldsymbol{v}}_{c_0} = \boldsymbol{0}$.

Equations (3.11), (3.12), and (3.13) are the scalar components of the Navier–Stokes equations, with the addition of a term similar to a body force, expressed in cylindrical coordinates in terms of the velocity vector $\tilde{\boldsymbol{u}}_0 = \tilde{\boldsymbol{v}}_{c_0} + \tilde{u}_0 \boldsymbol{e}_s$. The endolymphatic fluid velocity deviates from the velocity of the duct wall only by a small perturbation. The vector $\tilde{\boldsymbol{u}}_0$ represents this perturbation, as each of its components measures the velocity of the endolymph relative to the velocity of the duct wall when subjected to pure rotational motion. This being the case, any combination of products of any two of its components results in a quadratically small term. Neglecting such terms in (3.11), (3.12), and (3.13), we obtain the leading-order equations of motion, linearized about the velocity of the duct wall, given by

$$\frac{St}{Re}\frac{\partial \tilde{u}_0}{\partial t} - \frac{1}{Re}\tilde{\nabla}^2 \tilde{u}_0 + \frac{1}{2}\frac{\partial \tilde{p}_1}{\partial \bar{s}} = -\frac{St}{Re} R_p \ddot{\Omega}, \tag{3.14}$$

$$\frac{St}{Re}\frac{\partial \tilde{v}_{r_0}}{\partial t} - \frac{1}{Re}\left(\tilde{\nabla}^2 \tilde{v}_{r_0} - \frac{\tilde{v}_{r_0}}{r^2} - \frac{2}{r^2}\frac{\partial \tilde{v}_{\varphi_0}}{\partial \varphi}\right) + \frac{1}{2}\frac{\partial \tilde{p}_1}{\partial r} = 0, \tag{3.15}$$

$$\frac{St}{Re}\frac{\partial \tilde{v}_{\varphi_0}}{\partial t} - \frac{1}{Re}\left(\tilde{\nabla}^2 \tilde{v}_{\varphi_0} - \frac{\tilde{v}_{\varphi_0}}{r^2} + \frac{2}{r^2}\frac{\partial \tilde{v}_{r_0}}{\partial \varphi}\right) + \frac{1}{2r}\frac{\partial \tilde{p}_1}{\partial \varphi} = 0, \tag{3.16}$$

with the $O(1)$ boundary condition, $\tilde{\boldsymbol{u}}_0|_w = \boldsymbol{0}$.

The differential continuity equation expanded in powers of the slenderness ratio, ε, is given to $O(\varepsilon^2)$ by

$$\frac{\partial v_r}{\partial r} + \frac{v_r}{r} + \frac{1}{r}\frac{\partial v_\varphi}{\partial \varphi} + \left(v_r \cos\varphi - v_\varphi \sin\varphi + \frac{1}{2\pi}\frac{\partial v_s}{\partial s}\right) 2\pi\varepsilon + O(\varepsilon^2) = 0. \tag{3.17}$$

Thus, to leading order the differential continuity equation in the boundary layer is given by

$$\frac{\partial \tilde{v}_{r_0}}{\partial r} + \frac{\tilde{v}_{r_0}}{r} + \frac{1}{r}\frac{\partial \tilde{v}_{\varphi_0}}{\partial \varphi} + \frac{\partial \tilde{v}_{s_0}}{\partial \bar{s}} = 0. \tag{3.18}$$

To completely define the problem in the boundary layer, we need to specify kinematic boundary conditions on the surface of the cupula at $\bar{s} = 0$ and asymptotic matching conditions as $\bar{s} \to \pm\infty$. At the axial location of the cupula partition where $s = s_p$ and $\bar{s} = 0$, continuity requires that the velocity of the endolymph match that of the cupula. We therefore impose the kinematic boundary condition given by

$$\tilde{u}_0|_{\bar{s}=0} = \frac{\partial w_0}{\partial t}, \tag{3.19}$$

where $w_0(r,t)$ is the leading-order axisymmetric displacement of the cupula. In a transitional region, as $\bar{s} \to \pm\infty$, the boundary-layer solution must be made to asymptotically match the regular perturbation solution in the outer region. On one side of the cupula, the boundary layer and outer region meet when $\bar{s} \to \infty$ and $s \to 0$; on the other side the transition occurs as $\bar{s} \to -\infty$ and $s \to 1$. In passing from the boundary layer to the outer region, $\tilde{u}_0$ ceases to depend on $\bar{s}$ and we have the asymptotic matching condition

$$\lim_{\bar{s}\to\pm\infty} \frac{\partial^2 \tilde{u}_0}{\partial \bar{s}^2} \to 0. \tag{3.20}$$

In addition to these conditions on the axial velocity component, we impose the no-slip condition on the cross-sectional components of the velocity vector, $\tilde{\boldsymbol{v}}_c$, evaluated on the surface of the cupula at $\bar{s} = 0$. In general then, the radial and circumferential components, $\tilde{v}_{r_0}$ and $\tilde{v}_{\varphi_0}$, vanish at $\bar{s} = 0$. Finally, we impose the asymptotic matching condition between the boundary-layer and outer-region solutions which requires that the cross-sectional velocity components are $O(\varepsilon)$ as $\bar{s} \to \pm\infty$. These conditions are given to leading order by

$$\tilde{\boldsymbol{v}}_{c_0}(r,0,t) = \boldsymbol{0} \quad \text{and} \quad \lim_{\bar{s}\to\pm\infty} \tilde{\boldsymbol{v}}_{c_0}(r,\bar{s},t) = \boldsymbol{0}. \tag{3.21a,b}$$

An important observation to be made is the decoupling which occurs in the momentum equations in the special case of axisymmetric flow. Under these circumstances all derivatives with φ vanish and (3.14), (3.15), and (3.16) decouple so that $\tilde{v}_{r_0}$, $\tilde{v}_{\varphi_0}$, and $\tilde{u}_0$ can each be solved independently to an arbitrary function of integration. Furthermore, since the boundary condition on $\tilde{v}_{\varphi_0}$ is homogeneous and, in the axisymmetric case, the circumferential component of the pressure gradient vanishes, we see that $\tilde{v}_{\varphi_0}$ must also be identically zero. Axisymmetric flow in the boundary layer is therefore two-dimensional and we need only solve for the components $\tilde{v}_{r_0}$ and $\tilde{u}_0$ in order to determine the pressure, $\tilde{p}_1(r,\bar{s},t)$.

In the interest of clarity and continuity, the somewhat lengthy details of obtaining a solution to the velocity and pressure fields in the boundary layer are omitted. Only the primary results of the analysis are presented here. For a full discussion of these methods, see Damiano (1993). The axisymmetric solution to (3.14) and (3.15) is developed in detail there with only minor differences in notation.

3.1. *Axisymmetric solution for* $\tilde{u}_0$

To solve the inhomogeneous linear differential equation given by (3.14), we define a forcing function, $\tilde{g}(r,\bar{s})$, such that the pressure gradient and inertial forcing terms in

(3.14) can be expressed as

$$\tilde{g}(r,\bar{s})\,e^{it} = \frac{Re}{2}\frac{\partial \tilde{p}_1}{\partial \bar{s}} + St\,R_p\,\ddot{\Omega}. \tag{3.22}$$

Here we seek only the so-called transient-free solution and take $\ddot{\Omega} = -e^{it}$ for sinusoidal rotation. Since the problem is linear with homogeneous boundary conditions, we can construct an eigenfunction expansion to the solution $\tilde{u}_0$. The axisymmetric solution in the boundary layer for the axial velocity component, $\tilde{u}_0$, which satisfies (3.14) for $\bar{s} \geqslant 0$ is given by

$$\tilde{u}_0(r,\bar{s},t) = \sum_{n=1}^{\infty}\left\{\frac{\partial w_{0_n}}{\partial t}e^{-k_n\bar{s}} + e^{it}\left(b_n\sinh(k_n\bar{s}) - \frac{1}{k_n}\int_0^{\bar{s}}\tilde{g}_n(\sigma)\sinh\{k_n(\sigma-\bar{s})\}\,d\sigma\right)\right\}J_0(\alpha_n r), \tag{3.23}$$

where $k_n^2 = \alpha_n^2 + i\,St$, $\alpha_n = \beta_n/a_p$, and the eigenvalues, β_n, are the zeros of the zeroth-order Bessel function, J_0. The coefficients $\tilde{g}_n$ and w_{0_n} are defined as

$$\tilde{g}_n(\bar{s}) = \frac{\langle\tilde{g}(r,\bar{s}), J_{0_n}\rangle_\alpha}{\langle J_{0_n}, J_{0_n}\rangle_\alpha} \quad \text{and} \quad w_{0_n}(t) = \frac{\langle w_0(r,t), J_{0_n}\rangle_\alpha}{\langle J_{0_n}, J_{0_n}\rangle_\alpha}, \tag{3.24}$$

where the subscript α indicates that the argument of the Bessel functions in the inner products is $\alpha_n r$. Thus, the undetermined coefficients, $\tilde{g}_n(\bar{s})$, represent the s-dependent Fourier–Bessel coefficients of the function $\tilde{g}(r,\bar{s})$ expanded in terms of the modes of the fluid velocity vector's axial component. Similarly, $\partial w_{0_n}/\partial t$ represent the Fourier–Bessel coefficients of the velocity of the cupula partition expanded in terms of these same fluid modes. The constants b_n represent a countably infinite set of undetermined coefficients.

The inner products in (3.24) are defined with respect to the dimensionless local cross-sectional area of the duct, A. In the boundary layer, this has the expansion $A(\varepsilon\bar{s}) = A(0) + \varepsilon^2\bar{s}A'(0) + \cdots$. Similarly, the local cross-sectional radius, a, has the expansion in the boundary layer $a(\varepsilon\bar{s}) = a(0) + \varepsilon^2\bar{s}a'(0) + \cdots$. Thus to a leading-order approximation we take these parameters to be constant and equal to their values at the cupula partition. In the boundary layer then, a and A are approximated by $a(0) = a_p = a_p^*/a_0$ and $A(0) = A_p = A_p^*/(\pi a_0^2)$ where a_p^* and A_p^* are the dimensional radius and cross-sectional area of the cupula partition, respectively. We therefore define the eigenvalues in (3.23) by the constants $\alpha_n = \beta_n/(a_p^*/a_0)$. This implies that it is sufficient to use a uniform cross-section in the boundary layer.

The axial velocity component given by (3.23) was made to satisfy the kinematic boundary condition given by (3.19) whereas the asymptotic matching condition given by (3.20) imposes a restriction on $\tilde{g}_n$. In order to ensure that (3.23) asymptotically matches the outer-region solution in the transition from the boundary layer to the outer region, i.e. as $\bar{s} \to \infty$, we seek a solution $\tilde{g}_n(\bar{s})$ which satisfies

$$\lim_{\bar{s}\to\infty}\left\{b_n\sinh(k_n\bar{s}) - \frac{1}{k_n}\int_0^{\bar{s}}\tilde{g}_n(\sigma)\sinh\{k_n(\sigma-\bar{s})\}\,d\sigma\right\} = -\frac{g_n(0)}{k_n^2}, \tag{3.25}$$

in the positive limit.

3.2. *Axisymmetric solution for* $\tilde{v}_{r_0}$

In obtaining the axisymmetric solution to (3.15), we interpret the radial component of the pressure gradient as a forcing function which depends on r, $\bar{s}$, and t such that

$$\tilde{h}(r,\bar{s})\,e^{it} = \frac{Re}{2}\frac{\partial \tilde{p}_1}{\partial r}. \tag{3.26}$$

Since the problem is linear with homogeneous boundary conditions, we can construct an eigenfunction expansion to the solution $\tilde{v}_{r_0}$ just as was done for $\tilde{u}_0$. Analogous to (3.23), we obtain the axisymmetric solution in the boundary layer for the radial velocity component, $\tilde{v}_{r_0}$, which satisfies (3.15) for $\bar{s} \geqslant 0$ given by

$$\tilde{v}_{r_0}(r,\bar{s},t) = \sum_{n=1}^{\infty} e^{it}\left\{B_n \sinh(\kappa_n \bar{s}) - \frac{1}{\kappa_n}\int_0^{\bar{s}} \tilde{h}_n(\sigma)\sinh\{\kappa_n(\sigma-\bar{s})\}\,d\sigma\right\} J_1(\gamma_n r), \tag{3.27}$$

where $\kappa_n^2 = \gamma_n^2 + i\,St$, $\gamma_n = \delta_n/a_p$, and the eigenvalues, δ_n, are the zeros of the first-order Bessel function, J_1. The coefficients, $\tilde{h}_n$, are defined as

$$\tilde{h}_n(\bar{s}) = \frac{\langle \tilde{h}(r,\bar{s}), J_{1_n}\rangle_\gamma}{\langle J_{1_n}, J_{1_n}\rangle_\gamma}, \tag{3.28}$$

where the subscript γ indicates that the argument of the Bessel functions in the inner products is $\gamma_n r$. Analogous to $\tilde{g}_n(\bar{s})$, the undetermined coefficients $\tilde{h}_n(\bar{s})$ represent the s-dependent Fourier–Bessel coefficients of the function $\tilde{h}(r,\bar{s})$ expanded in terms of the modes of the fluid velocity vector's radial component while the constants B_n represent a countably infinite set of undetermined coefficients.

The radial velocity component given by (3.27) was made to satisfy the boundary condition given by (3.21*a*) whereas the asymptotic matching condition given by (3.21*b*) imposes a restriction on $\tilde{h}_n$. In order to ensure that (3.27) satisfies the asymptotic matching condition in the transition from the boundary layer to the outer region, i.e. as $\bar{s} \to \infty$, we seek a solution $\tilde{h}_n(\bar{s})$ which satisfies

$$\lim_{\bar{s}\to\infty}\left\{B_n \sinh(\kappa_n \bar{s}) - \frac{1}{\kappa_n}\int_0^{\bar{s}} \tilde{h}_n(\sigma)\sinh\{\kappa_n(\sigma-\bar{s})\}\,d\sigma\right\} = 0, \tag{3.29}$$

in the positive limit.

3.3. *The pressure gradient and velocity vectors in the boundary layer*

At this point, the velocity and pressure fields are known to within two arbitrary sets of constants, b_n and B_n, and two sets of functions $\tilde{g}_n(\bar{s})$ and $\tilde{h}_n(\bar{s})$ (in addition to the Fourier–Bessel coefficients w_{0_n} which must be determined from the momentum equation for the cupula). These unknowns are subject to the two asymptotic matching conditions given by (3.25) and (3.29). For closure, two more equations are necessary. One of these comes from a compatibility condition which is obtained by requiring that the mixed partial derivative of $\tilde{p}_1$ with respect to r and $\bar{s}$ commutes. Differentiating (3.22) with respect to r and (3.26) with respect to $\bar{s}$, we obtain the compatibility condition

$$\frac{\partial \tilde{h}}{\partial \bar{s}} = \frac{\partial \tilde{g}}{\partial r}. \tag{3.30}$$

For the remaining equation we invoke the continuity equation. In the axisymmetric case, the differential continuity equation given by (3.18) depends only on $\tilde{v}_{r_0}$ and $\tilde{v}_{s_0}$.

Since $\partial \tilde{v}_{s_0}/\partial \bar{s} = \partial \tilde{u}_0/\partial \bar{s}$, we have for axisymmetric flow

$$\frac{\partial \tilde{v}_{r_0}}{\partial r} + \frac{\tilde{v}_{r_0}}{r} + \frac{\partial \tilde{u}_0}{\partial \bar{s}} = 0. \tag{3.31}$$

By making use of these equations, we can reduce the number of unknowns. The solution of the continuity equation (3.31), subject to the compatibility condition (3.30) and the integral equations (3.25) and (3.29), determines the constants of integration $\tilde{g}$ and $\tilde{h}$ to within the unknown harmonically time-dependent constants, w_{0_n}. An additional equation governing the displacement of the cupula (see the Appendix) will provide the final equation necessary to determine these constants and thus achieve closure for the model. If we substitute the Fourier–Bessel series representations of $\tilde{g}$ and $\tilde{h}$ into the compatibility condition given by (3.30), we obtain

$$\sum_{n=1}^{\infty} \tilde{h}_n' J_1(\gamma_n r) = \sum_{n=1}^{\infty} -\alpha_n \tilde{g}_n J_1(\alpha_n r). \tag{3.32}$$

Since there exists no function which is mutually orthogonal to $J_1(\gamma_n r)$ and $J_1(\alpha_n r)$ the infinite summations in (3.32) cannot be made to simultaneously collapse. We are confronted with the same obstacle if we use (3.31). In order to reduce the number of unknowns then, we assume the simplest admissible solution form for the coefficients $\tilde{h}_n$ which satisfies the integral equation given by (3.29). In a similar way we assume a solution form for the coefficients $\tilde{g}_n$ which satisfies the integral equation given by (3.25) and which can be made consistent with our compatibility condition given by (3.30). With the functions $\tilde{g}_n$ and $\tilde{h}_n$ known each to an arbitrary set of constants, we impose the differential continuity equation (3.31) which results in an expression allowing us to obtain a relationship between the constants associated with $\tilde{g}_n$ and the unknown Fourier–Bessel coefficients w_{0_n}. Finally, since we only require the pressure differential across the cupula, we obtain an expression for the pressure on the opposite side of the cupula, i.e. where $\bar{s} \leqslant 0$, and determine the difference. We find that terms containing the unknown constants of integration cancel on both sides of the cupula leaving us with an expression relating the pressure differential to the amplitudes of the cupula partition's velocity, $\partial w_{0_n}/\partial t$, expanded in terms of the fluid modes. This result is easily incorporated into a Galerkin approximation (see § 5) or a finite element model to determine the response of the cupula to sinusoidal rotation.

In constructing the solution form for $\tilde{g}(r, \bar{s})$ and $\tilde{h}(r, \bar{s})$ (Damiano 1993), we determine the $\bar{s}$-dependence throughout the boundary layer to a two-fold infinity of unknown constants denoted by B_n and K_{3_n} (in addition to the unknown Fourier–Bessel coefficients w_{0_n}). The resulting components of the pressure gradient and velocity vectors for $\bar{s} \geqslant 0$ are given by

$$\frac{\partial \tilde{p}_1}{\partial r} = -\frac{8\,\mathrm{e}^{\mathrm{i}t}}{Re} \sum_{n=1}^{\infty} B_n \kappa_n^3 \bar{s}\, \mathrm{e}^{-\kappa_n \bar{s}} J_1(\gamma_n r), \tag{3.33}$$

$$\frac{\partial \tilde{p}_1}{\partial \bar{s}} = -\frac{4}{Re} \sum_{n=1}^{\infty} \left\{ k_n^2 \frac{\partial w_{0_n}}{\partial t} + \mathrm{e}^{\mathrm{i}t} \left(g_n(0) + \frac{K_{3_n}}{4k_n} - \frac{K_{3_n}}{2} \bar{s} \right) \right\} \mathrm{e}^{-k_n \bar{s}} J_0(\alpha_n r), \tag{3.34}$$

$$\tilde{v}_{r_0}(r, \bar{s}, t) = \sum_{n=1}^{\infty} B_n \kappa_n (\bar{s} + \kappa_n \bar{s}^2)\, \mathrm{e}^{-\kappa_n \bar{s} + \mathrm{i}t} J_1(\gamma_n r), \tag{3.35}$$

and

$$\tilde{u}_0(r,\bar{s},t)=\sum_{n=1}^{\infty}\left\{(k_n\bar{s}+1)\frac{\partial w_{0_n}}{\partial t}e^{-k_n\bar{s}}\right.$$

$$\left.-\frac{g_n(0)\,e^{it}}{k_n^2}+\frac{e^{-k_n\bar{s}+it}}{k_n^2}\left(g_n(0)(1+k_n\bar{s})-\tfrac{1}{4}K_{3_n}k_n\bar{s}^2\right)\right\}J_0(\alpha_n r). \tag{3.36}$$

3.4. *The pressure differential,* $\Delta\tilde{p}_1$

With the goal of determining an expression for the pressure differential acting across the cupula, we seek to determine an expression similar to (3.34) for $\bar{s}\leqslant 0$. Following the same procedure as before, we find that the axial component of the pressure gradient on the side of the cupula where $\bar{s}\leqslant 0$ is given by

$$\frac{\partial\tilde{p}_1}{\partial\bar{s}}=\frac{4}{Re}\sum_{n=1}^{\infty}\left\{k_n^2\frac{\partial w_{0_n}}{\partial t}+e^{it}\left(g_n(1)+\frac{K_{3_n}}{4k_n}+\frac{K_{3_n}}{2}\bar{s}\right)\right\}e^{k_n\bar{s}}J_0(\alpha_n r), \tag{3.37}$$

where $g_n(1)=-g_n(0)$ is required by the asymptotic matching condition given by (3.25). This result is not unexpected since, in the outer region, integral continuity given by (2.18) requires that at any instant in time the total volume flow at every cross-section is constant. Since the cross-section of the duct in the boundary layer is taken to be uniform, the amplitude of the velocity profile where the boundary layer meets the outer region at $s=0$ (on the horizontal-canal side of the cupula) must equal the amplitude at $s=1$ (on the utricular side of the cupula).

In order to find the pressure differential acting across the cupula, we integrate (3.34) and (3.37) with respect to $\bar{s}$ and thereby obtain expressions for the pressure drop on each side of the cupula. The difference in these at a fixed distance $|\bar{s}|$ away from the cupula represents the pressure differential across the cupula as a result of only a portion of the boundary layer: that corresponding to the region extending a distance $|\bar{s}|$ into the boundary layer on both sides of the cupula. Passing to the limit then, as $|\bar{s}|\to\infty$, we obtain the pressure differential acting across the cupula as a result of the cumulative effect of the entire boundary layer. Upon integration of (3.34) and (3.37) with respect to $\bar{s}$, the expressions for the pressure drop on the side of the cupula corresponding to $\bar{s}\geqslant 0$ and $\bar{s}\leqslant 0$ are given respectively by

$$\tilde{p}_1(\bar{s}^+)-\tilde{p}_1(0^+)=\frac{4}{Re}\sum_{n=1}^{\infty}\left\{\left(k_n\frac{\partial w_{0_n}}{\partial t}+\frac{g_n(0)\,e^{it}}{k_n}\right)(e^{-k_n|\bar{s}|}-1)\right.$$

$$\left.+e^{it}\left(\frac{K_{3_n}}{4k_n^2}(1-e^{-k_n|\bar{s}|}-2k_n|\bar{s}|\,e^{-k_n|\bar{s}|})\right)\right\}J_0(\alpha_n r), \tag{3.38}$$

and

$$\tilde{p}_1(\bar{s}^-)-\tilde{p}_1(0^-)=-\frac{4}{Re}\sum_{n=1}^{\infty}\left\{\left(k_n\frac{\partial w_{0_n}}{\partial t}-\frac{g_n(0)\,e^{it}}{k_n}\right)(e^{-k_n|\bar{s}|}-1)\right.$$

$$\left.-e^{it}\left(\frac{K_{3_n}}{4k_n^2}(1-e^{-k_n|\bar{s}|}-2k_n|\bar{s}|\,e^{-k_n|\bar{s}|})\right)\right\}J_0(\alpha_n r), \tag{3.39}$$

where $\bar{s}^+$ indicates $\bar{s}\geqslant 0$ and $\bar{s}^-$ indicates $\bar{s}\leqslant 0$. Subtracting (3.39) from (3.38),

we obtain

$$\Delta\tilde{p}_1(r,|0|,t) = \Delta\tilde{p}_1(r,|\bar{s}|,t) - \frac{8}{Re}\sum_{n=1}^{\infty} k_n \frac{\partial w_{0_n}}{\partial t}(1-\mathrm{e}^{-k_n|\bar{s}|})J_0(\alpha_n r), \tag{3.40}$$

where

$$\Delta\tilde{p}_1(r,|\bar{s}|,t) = \tilde{p}_1(r,\bar{s}^-,t) - \tilde{p}_1(r,\bar{s}^+,t). \tag{3.41}$$

The difference (from one side of the cupula to the other) in the pressure drop from the surface of the cupula to a distance $|\bar{s}|$ away from the cupula is given by (3.40). In order to obtain the pressure differential across the cupula due to the cumulative effect of the entire boundary layer, we must consider the transcupular difference in the pressure drop through the boundary layer, from the surface of the cupula (at $|\bar{s}| = 0$) to the outer region (as $|\bar{s}| \to \infty$). Passing to the limit then, as $|\bar{s}| \to \infty$, we obtain

$$\Delta\tilde{p}_1(r,|0|,t) = \Delta\tilde{p}_1(r,|\infty|,t) - \frac{8}{Re}\sum_{n=1}^{\infty} k_n \frac{\partial w_{0_n}}{\partial t} J_0(\alpha_n r). \tag{3.42}$$

From (3.4) we can write

$$\Delta\tilde{p}(r,|0|,t) \sim \Delta\tilde{p}_0(|\infty|,t) + \varepsilon\,\Delta\tilde{p}_1(r,|0|,t) + \cdots, \tag{3.43}$$

where we have taken $\Delta\tilde{p}_0(|0|,t) = \Delta\tilde{p}_0(|\infty|,t)$ since $\tilde{p}_0$ is constant with respect to $\bar{s}$ in the boundary layer. Substituting for $\Delta\tilde{p}_1(r,|0|,t)$ from (3.42) into the expansion for $\Delta\tilde{p}$ from above we obtain

$$\Delta\tilde{p}(r,|0|,t) \sim \Delta\tilde{p}_0(|\infty|,t) + \varepsilon\,\Delta\tilde{p}_1(r,|\infty|,t) - \frac{8\varepsilon}{Re}\sum_{n=1}^{\infty} k_n \frac{\partial w_{0_n}}{\partial t} J_0(\alpha_n r) + \cdots. \tag{3.44}$$

In terms of the actual velocity of the cupula partition, the pressure differential across the cupula has the asymptotic form given by

$$\Delta p(r,t) \sim \Delta p_0 - \frac{8\varepsilon}{Re}\sum_{n=1}^{\infty} (\alpha_n^2 + \mathrm{i}\,St)^{1/2} \frac{\langle \frac{\partial w_0}{\partial t}, J_{0_n}\rangle_\alpha}{\langle J_{0_n}, J_{0_n}\rangle_\alpha} J_0(\alpha_n r) + \cdots. \tag{3.45}$$

Combining this with the $O(1)$ solution obtained from the outer region given by (2.14) provides the relatively simple expression, given in the Introduction in dimensional form, for the pressure differential across the cupula. In non-dimensional form this is given by

$$\begin{aligned}\Delta p \sim -2\frac{St}{Re}\left\{\int_0^1 \ddot{\boldsymbol{\Omega}} \times \boldsymbol{R}\cdot \mathrm{d}\boldsymbol{s}_\circ + \int_0^1 \frac{\boldsymbol{n}\cdot\mathrm{d}\boldsymbol{s}_\circ}{A}\iint_{A_p}\frac{\partial^2 w_0}{\partial t^2}\mathrm{d}A\right\}\\ -\frac{2}{Re}\int_0^1 \frac{\lambda}{A^2}\boldsymbol{n}\cdot\mathrm{d}\boldsymbol{s}_\circ \iint_{A_p}\frac{\partial w_0}{\partial t}\mathrm{d}A - \frac{8\varepsilon}{Re}\sum_{n=1}^{\infty}(\alpha_n^2+\mathrm{i}\,St)^{1/2}\frac{\langle\frac{\partial w_0}{\partial t}, J_{0_n}\rangle}{\langle J_{0_n}, J_{0_n}\rangle}J_0(\alpha_n r) + \cdots,\end{aligned} \tag{3.46}$$

where we have dropped the subscript α to the inner products and hereafter J_{0_n} will imply $J_0(\alpha_n r)$. The result assumes that the endolymph is Newtonian and the endolymphatic duct and ampulla are rigid. No assumptions are made with regard to the cupula and the expression implicitly includes its deformation field. From (3.46) we see that the pressure differential acting across the cupula arises from four sources:

inertial forcing, endolymphatic mass and viscous loading on the cupula, and the multi-dimensional fluid dynamics within the ampulla.

4. Simple model for the cupula: an example

The cupular boundary condition (3.46) reduces the mechanics of endolymph flow and pressure for the entire canal to a dynamic boundary condition acting on the two leaflet surfaces of the cupula. Because of this the differential pressure can easily be incorporated into finite-element or similar numerical models describing cupular dynamics. In order to demonstrate this for a complete semicircular canal system, we couple the pressure differential to a simple viscoelastic membrane model of the cupula and solve the resulting equations numerically.

Direct measurements of the mechanical properties of the cupula and its frequency-dependent deformation field do not appear in the literature and hence we rely upon indirect evidence to construct a model. Our approach in the present work is to employ the simplest model adequate to demonstrate the significance of the fluid–structure interaction. Such a minimal model should also be consistent with the limited experimental data available to date. There is experimental evidence suggesting that the cupula (i) has stiffness and resists deformation from its resting position, (ii) has viscosity and resists the rate of change of deformation from the resting position, and (iii) has a spatially non-uniform deflection field. Evidence of stiffness is provided by the lower corner frequency observed in the afferent responses of numerous species (Blanks *et al.* 1975; Boyle & Highstein 1990; Fernández & Goldberg 1971; Hartmann & Klinke 1980; Landolt & Correia 1980; Segalönbein & Outerbridge 1982) and by observation of the cupula deflection resulting from static pressures (McLaren & Hillman 1979). Upon suction-pipette removal of the cupula from the ampulla, the cupula maintains some coherence when placed on a glass slide and moves as a deforming mass under mechanical probing. Coherence suggests the existence of at least some mechanical stiffness. In this manipulation however, the original geometry of the cupula is completely lost indicating that prestress is present *in vivo*. Also under *in situ* observation, the cupula appears to be highly viscous relative to the endolymph. This qualitative observation of viscosity is supported by measurements of the phase of endolymph pressure modulations recorded within the semicircular canal ampulla (Rabbitt, Boyle & Highstein 1995*b*). Finally, spatial non-uniformity of the deflection field is evidenced by the organized spatial distribution of afferent projections in the crista (Boyle, Carey & Highstein 1991; Goldberg, Lysakowski & Fernández 1992) and by the diaphragm-like deflection field of the cupula observed under static pressure excitation recorded by McLaren & Hillman (1979).

Consistent with the above observations we employ a minimal model of the cupula that has restoring force, prestress, viscosity, and spatial extent. For simplicity, the prestress and restoring force are achieved using a simple elastic membrane model. The restoring force associated with the membrane model appears in the resulting stiffness matrix and hence is termed 'stiffness'. In reality, the cupula probably has a combination of elastic and prestress restoring mechanisms. As noted later however, numerical results are similar for these two restoring mechanisms and hence we have elected to use the simpler of the two for the present example calculation. Viscosity is included using a linear Newtonian mechanism. Since the endolymph is also modelled as Newtonian, matching the viscosities and letting the cupular stiffness approach zero has the effect of replacing the cupula with endolymph. Such a limit allows

investigation of the unsteady fluid dynamics within the ampulla in the presence of, or in the absence of, the cupula using a single numerical code.

The model cupula completely spans the cross-section of the ampulla. It is a relatively thick structure but is reduced here to two dimensions by assuming uniform deformation through the thickness. Clearly this is a highly restrictive assumption and prevents direct application of this cupula model to mammalian species where the cupula is inherently three-dimensional and extends down the curved sides of the crista. In the present example, we apply the model to the geometry of the toadfish canal in which the sensory epithelium is two-dimensional and the surface between the cupula and the crista is relatively flat (Boyle *et al.* 1991). The cupular boundary condition given by (3.46) is not restricted by this simplification and can be applied to more general three-dimensional models of the cupula. Since this work is focused primarily on the multi-dimensional fluid dynamics, in this initial work we apply the boundary condition to a simple two-dimensional model of cupular dynamics. The cupula model is written in a form valid for any cross-sectional shape. Specific numerical results are provided only for the axisymmetric case where the cupula is further simplified to have a circular boundary. Relaxing these assumptions remains a subject of future work.

We arrive at the coupled model by substituting the pressure differential given by (3.46) into the simple cupular model given by (A 2) in the Appendix to obtain

$$\frac{St}{Re}\left(\int_0^1 \frac{\boldsymbol{n}\cdot\mathbf{d}\boldsymbol{s}_\circ}{A}\iint_{A_p}\frac{\partial^2 w_0}{\partial t^2}\mathrm{d}A+\frac{h/l}{\rho/\rho_p}\frac{\partial^2 w_0}{\partial t^2}\right)$$

$$+\frac{1}{Re}\left(\int_0^1 \frac{\lambda}{A^2}\boldsymbol{n}\cdot\mathbf{d}\boldsymbol{s}_\circ\iint_{A_p}\frac{\partial w_0}{\partial t}\mathrm{d}A-\frac{h/l}{\mu/\mu_p}\nabla_c^2\left(\frac{\partial w_0}{\partial t}\right)\right)$$

$$+\frac{4\varepsilon}{Re}\sum_{n=1}^{\infty}\left(\alpha_n^2+\mathrm{i}\,St\right)^{1/2}\frac{\langle\partial w_0/\partial t, J_{0_n}\rangle}{\langle J_{0_n}, J_{0_n}\rangle}J_0(\alpha_n r)-\nabla_c\cdot(\psi\nabla_c w_0)$$

$$=-\frac{St}{Re}\left(\int_0^1 \ddot{\boldsymbol{\Omega}}\times\boldsymbol{R}\cdot\mathbf{d}\boldsymbol{s}_\circ+\frac{h/l}{\rho/\rho_p}R_p\ddot{\Omega}\right), \tag{4.1}$$

subject to the fixed boundary conditions imposed on the cupula given by (A 3).

5. Example numerical solution

To solve this equation we employ the numerical method of weighted residuals attributed to Galerkin. We limit our attention to sinusoidal motion and approximate the transient-free axisymmetric deformation field of the cupula by the series

$$w_0(r,t)\approx \mathrm{e}^{\mathrm{i}t}\sum_{n=1}^{N}X_n\,q_n(r), \tag{5.1}$$

where $q_n(r)$ are comparison functions meeting the geometric or essential boundary conditions of the partition (Reddy 1984). Substituting this approximation into (4.1), multiplying by $q_m(r)$, and integrating over the cross-section provide a linear $N\times N$ system of equations. When solved for the amplitudes, X_n, we have the following matrix form:

$$\vec{X}=(-\boldsymbol{M}+\mathrm{i}\boldsymbol{C}+\boldsymbol{K})^{-1}\vec{F}, \tag{5.2}$$

where $\vec{X}$ and $\vec{F}$ are column vectors containing the elements X_n and F_n and $\boldsymbol{M}$, $\boldsymbol{C}$, and $\boldsymbol{K}$ are the mass, damping, and stiffness matrices, respectively. The elements of the matrix coefficients and the forcing vector, $\vec{F}$, are

$$M_{mn} = \frac{St}{Re}\left(\int_0^1 \frac{\boldsymbol{n}\cdot\mathbf{ds}_\circ}{A}\langle 1, q_m\rangle\langle 1, q_n\rangle + \frac{h/l}{\rho/\rho_p}\langle q_m, q_n\rangle\right), \tag{5.3}$$

$$C_{mn} = \frac{1}{Re}\left(\int_0^1 \frac{\lambda}{A^2}\boldsymbol{n}\cdot\mathbf{ds}_\circ\,\langle 1, q_m\rangle\langle 1, q_n\rangle - \frac{h/l}{\mu/\mu_p}\langle q_m, \nabla_c^2 q_n\rangle\right) + \frac{4\varepsilon}{Re}\sum_{j=1}^{J}\left(\alpha_n^2 + \mathrm{i}\,St\right)^{1/2}\frac{\langle q_m, J_{0_j}\rangle\langle q_n, J_{0_j}\rangle}{\langle J_{0_j}, J_{0_j}\rangle}, \tag{5.4}$$

$$K_{mn} = -\langle q_m, \nabla_c\cdot(\psi\nabla_c q_n)\rangle, \tag{5.5}$$

$$F_n = \frac{St}{Re}\left(\int_0^1 \frac{\ddot{\boldsymbol{\Omega}}}{\ddot{\Omega}}\times\boldsymbol{R}\cdot\mathbf{ds}_\circ + \frac{h/l}{\rho/\rho_p}R_p\right)\langle 1, q_n\rangle, \tag{5.6}$$

where we have truncated the infinite sum associated with the boundary layer to J terms. The integral coefficients appearing in the mass, viscous, and inertial forcing terms were determined numerically for the toadfish geometry and are reported in dimensionless form in table 1.

6. Theoretical results

6.1. *Spatially averaged results*

Results for the deflection of the cupula averaged over the ampullary cross-section are provided in figure 4. The practice of vestibular physiologists is to show the response to sinusoidal rotational stimulation in the form of Bode plots. In this format the gain of cupular displacement is defined with respect to the peak angular velocity of the head. The convention adopted for the phase is that a quantity with zero phase is aligned with head velocity, a 90° phase lead (+90°) is aligned with head acceleration, and a 90° phase lag (−90°) is aligned with head displacement. In figure 4, panels (*a*) and (*b*) show the gain and phase of the spatially averaged cupula deflection and (*c*) and (*d*) show the gain and phase of the spatially averaged transcupular pressure, respectively. The spatially averaged transcupular pressure is defined as the average pressure acting on the canal-lumen side of the cupula minus that on the utricular side.

Results for the spatially averaged deflection of the cupula are in quantitative agreement with previous morphologically descriptive models (Oman *et al.* 1987; Damiano 1993). The spatially averaged transcupular pressure is also in quantitative agreement with previous work (Rabbitt *et al.* 1994). This agreement holds even though previous models completely ignore the boundary-layer term. The reason stems from the fact that the outer-region analysis entirely captures the spatially averaged pressure acting across the cupula and the boundary layer only contributes to spatial variations. Hence, when we average across the surface of the cupula the boundary layer does not contribute. In contrast, the boundary layer is fundamental to the role the endolymph plays in entraining the motion of a local point on the cupula with the neighbouring regions and to the spatially dependent results described below.

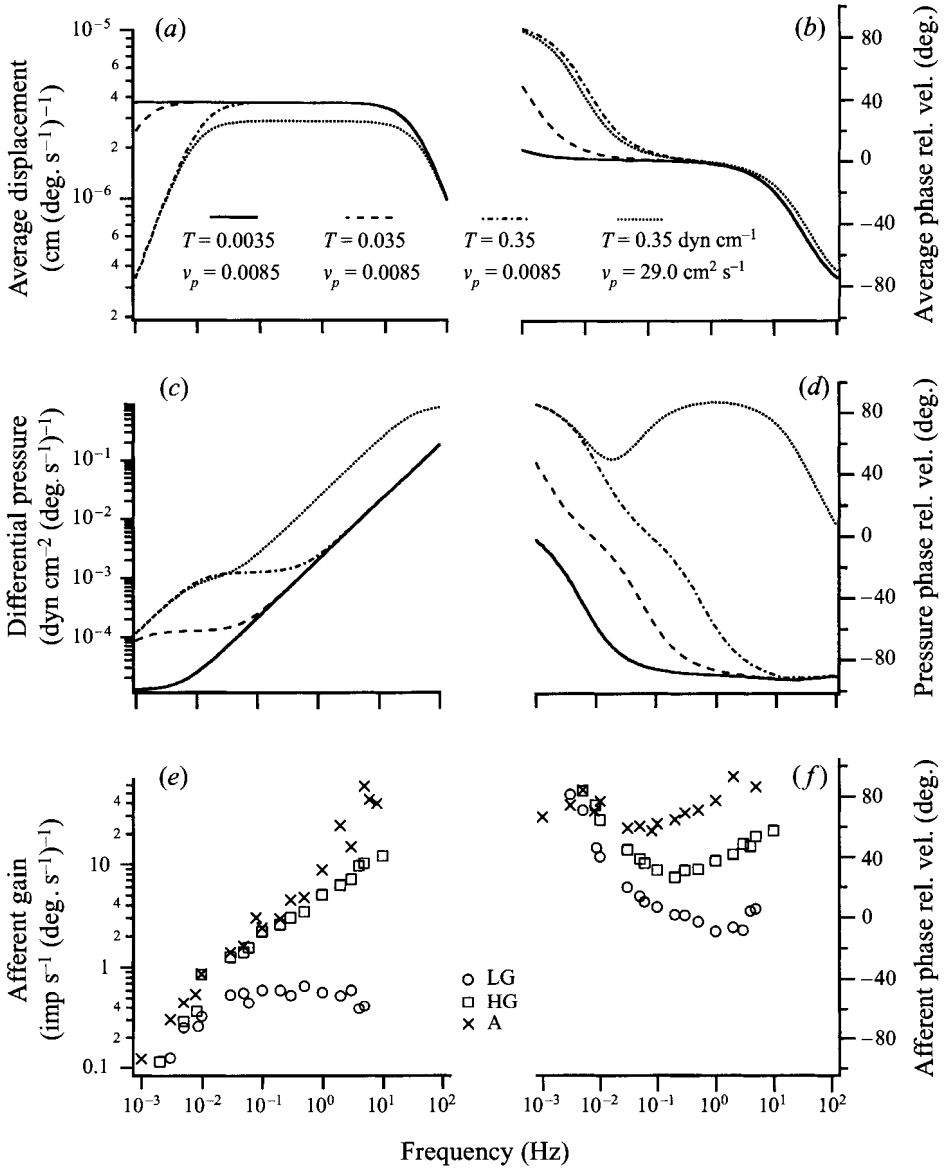

FIGURE 4. The frequency response predicted by the outer-region model, when the ampullary boundary layer is ignored, is shown here for the toadfish geometry in the form of Bode plots. Results give the average displacement gain (*a*) and phase (*b*) of the cupula and differential pressure gain (*c*) and phase (*d*) across the cupula relative to the angular velocity of the head. For comparison, afferent response data for low-gain (LG), high-gain (HG), and acceleration (A) type units, as reported by Boyle & Highstein (1990) in the toadfish, are also shown in (*e*) and (*f*). A stiffness of 0.35 dyn cm^{-1} is shown to produce the same lower corner frequency as measured on the vestibular nerve. The higher corner frequency which appears in the average displacement gain is independent of the stiffness and occurs at about 20 Hz. These results supersede the spatially averaged gain and phase given by Rabbitt & Damiano (1992) which contain a numerical error that is corrected here.

6.2. *Spatially dependent results*

The principal analytical result of the present work is to lump the three-dimensional endolymphatic fluid dynamics into a two-dimensional boundary condition that relates the pressure across the cupula to the motion of the cupula. This boundary condition is given in non-dimensional form by (3.46) and in dimensional form by (1.1). It includes the three-dimensional morphology of the endolymphatic duct, the unsteady fluid dynamics throughout the entire duct, and the multi-dimensional fluid–structure interaction at the cupula.

The boundary-layer part of the endolymph–cupula interaction is crucial to the ability to address the pointwise displacement field of the cupula or the local stimulation of the stereociliary bundles. This is illustrated by results for the gain and phase of the cupular shear angle at the interface with the crista which provides a local measure of cupula deflection relevant to the deflection of the hair bundles. The shear angle shows strong sensitivity to the boundary layer that is completely absent in the spatially averaged results, especially in the high-physiological frequency range. Figure 5 shows the cupular shear angle computed at the crista for several values of stiffness. Notice the increase in the local gain and phase above 1 Hz that is absent in the spatially averaged results (figure 4). These results correspond to an axisymmetric cupula, so this example does not address spatial diversity along the surface of the crista but simply illustrates the fundamental difference between the local and spatially averaged results.

The increasing importance of the boundary layer with increasing frequency is also evidenced by the boundary-layer thickness shown in figure 6. Recall from (3.40) that the multi-dimensional differential pressure distribution through the boundary layer decays exponentially as the distance from the cupula is increased in proportion to $e^{-\mathrm{Re}(\hat{k}_n|\bar{s}|)}$. We can use this fact to determine the effective normalized thickness of the boundary layer, t_b^*/a_p^*, from the area under the exponentially decaying curve to arrive at

$$t_b^*/a_p^* = \frac{2^{3/2}}{\left(\beta_n^2 + \left(\beta_n^4 + St_p^2\right)^{1/2}\right)^{1/2}}, \tag{6.1}$$

where St_p is defined with respect to a_p^*, the radius of the ampulla at the cross-sectional location corresponding to the cupula. In addition to the frequency, the length of the boundary layer depends on the cross-sectional radius of the ampulla, on the endolymphatic viscosity, and on the eigenvalues of the viscous fluid modes. Figure 6 shows the normalized boundary-layer thickness, t_b^*/a_p^*, on one side of the cupula plotted as a function of frequency. The boundary-layer thickness associated with the first and second fluid modes decreases markedly as the frequency is increased. As a consequence, the rate at which the velocity profile changes through the boundary layer increases with frequency as does the associated magnitude of the viscous shear stress. This stress is further amplified by increased spatial complexity of the cupular deformation field with increasing frequency. It is precisely this increase in viscous shear stress that makes it necessary to include the ampullary boundary layer at higher frequencies.

7. Discussion

7.1. *The cupular boundary condition*

The principal result of the current work is the derivation of the cupular boundary condition given by (1.1). From a complicated system of differential equations, this result extracts four relatively simple terms having clear morpho-physiological origins.

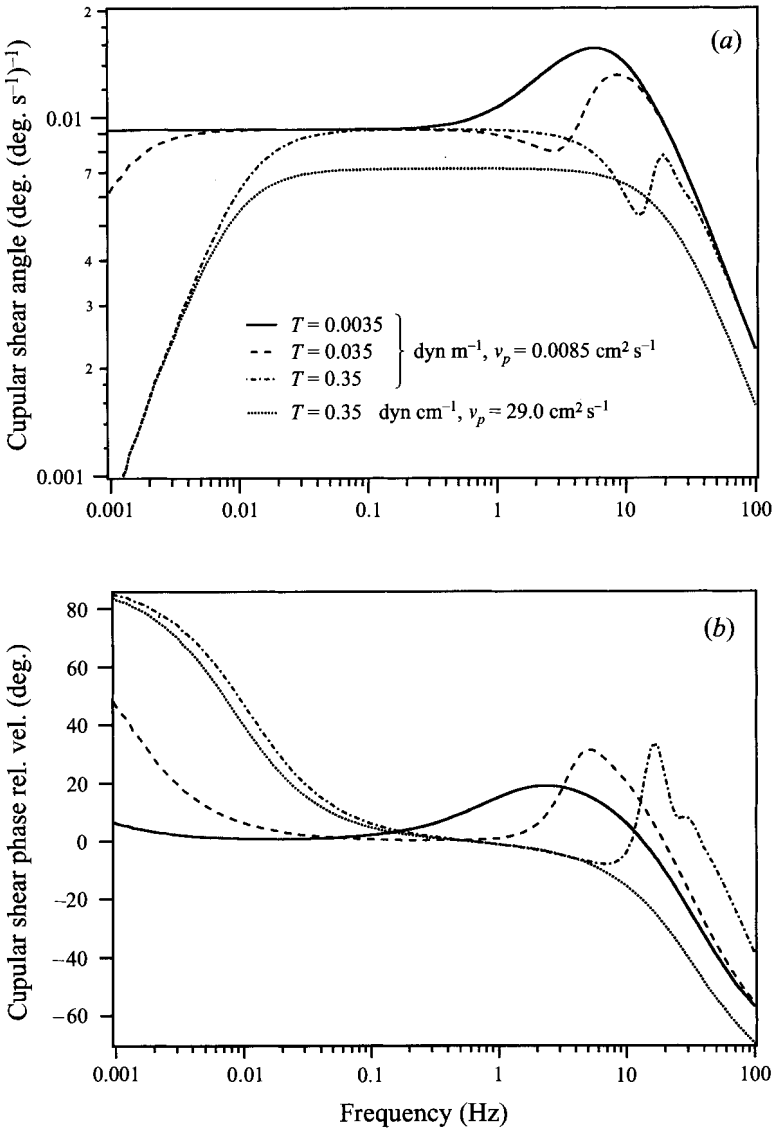

FIGURE 5. The response of the horizontal semicircular canal of the toadfish as predicted by the model, including the contribution of the boundary layer, is shown in terms of Bode plots of (*a*) the gain and (*b*) the phase of the cupular shear angle at the crista. Results show that the pointwise response is significantly influenced by the boundary layer but the spatially averaged cupular gain and phase are not – i.e. spatially averaged macromechanical results including the boundary layer are identical to the outer-region results that completely ignore the ampullary boundary layer (figure 4). For a cupular membrane stiffness below 0.035 dyn cm^{-1}, the viscous drag due to the boundary layer significantly influences the dynamics of the cupula whereas a higher cupular stiffness constrains the velocity profile of the fluid in the boundary layer and reduces the influence of the boundary layer. For a cupular viscosity several orders of magnitude greater than the endolymph, the influence of the boundary layer is overwhelmed by the dissipation in the cupula. In this case, the gain and phase of the pointwise response is qualitatively the same as the spatially averaged response including the location of the upper and lower corner frequencies.

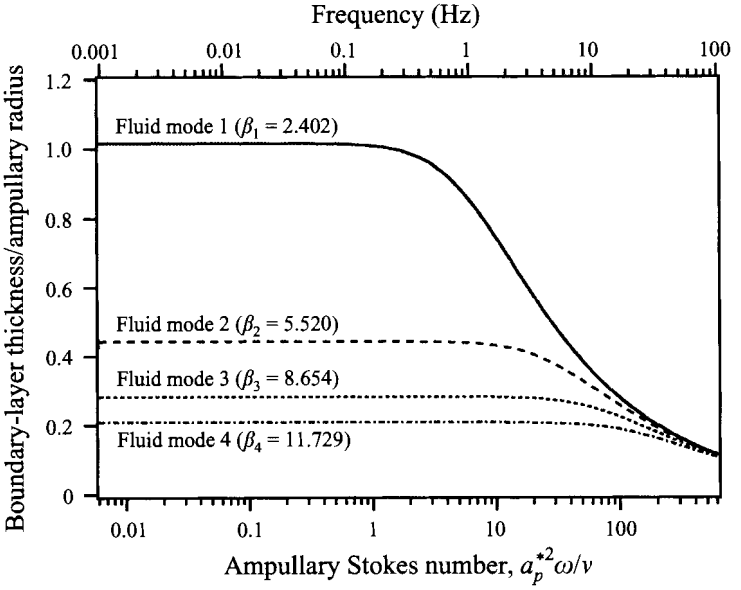

FIGURE 6. The boundary-layer thickness, t_b^*, as given by (6.1) and scaled by the radius of the ampulla, a_p^*, is shown as a function of frequency and the ampullary Stokes number for the first four fluid modes. The curves show the normalized boundary-layer thickness, t_b^*/a_p^*, on one side of the cupula; another boundary layer of equal thickness exists on the other side. As the frequency increases, the thickness of the boundary layer decreases. This means that the velocity profile changes over a shorter distance and as a result the viscous shear stress in the boundary layer increases significantly with frequency.

The first term, denoted by Δp_i^*, is the inertial forcing resulting from the acceleration of the endolymphatic duct wall which is proportional to the angular acceleration of the head, $\ddot{\Omega}^*$. The magnitude of this term depends upon the integral over the length of the duct of the projection of the tangential acceleration, $\ddot{\Omega}^* \times \boldsymbol{R}^*$, in the direction of the duct wall. The expression for Δp_i^*, given by (1.2), is valid for any rigid-body motion of the head. Notice that the inertial forcing coefficient is independent of the local cross-sectional shape of the duct but depends locally on the distance between the duct wall and the axis of rotation. The inertial forcing arising from the acceleration of the duct wall is analogous to a time-dependent body force. As such, it acts on the endolymph much in the same way that a gravitational force acts on a column of fluid where the hydrostatic pressure depends only on depth and is independent of the shape of the container. Since the cupula deflects, allowing endolymph flow relative to the motion of the duct wall, Δp_i^* is slightly greater than the differential pressure across the cupula. This difference is accounted for by pressure losses arising from endolymphatic mass and viscous loading on the cupula.

The effective mass loading, Δp_m^*, is equal to the component of the mass acceleration of a differential length of endolymph integrated over the length of the duct and weighted by the local inverse cross-sectional area. The inverse-area dependence appearing in Δp_m^* is accounted for by recognizing that the endolymphatic mass loading on the cupula is related to the kinetic energy of the endolymph moving relative to the head. Since the volume flow over every cross-section is equal, the *relative* fluid velocity, and its associated kinetic energy, is much greater in the long-and-slender portion of the duct than in the utricle where the cross-sectional area is

larger. Thus the contribution from the endolymph in the long-and-slender portion of the duct dominates the effective mass loading on the cupula.

The viscous drag arising between the endolymphatic fluid and the duct wall induces an additional pressure drop along the length of the duct. This generates an effective viscous loading on the cupula and is given by Δp_v^*. The drag depends on the geometry of the duct, the volumetric flow rate, and the shape of the velocity profile. The effective viscous loading is inversely proportional to the square of the local cross-sectional area of the duct. Similar to the effective mass loading, the long-and-slender portion of the duct also dominates the effective viscous loading on the cupula. Owing to its large cross-sectional area, the viscous drag in the utricle is small and does not contribute significantly to the differential pressure across the cupula.

For oscillatory flow in the horizontal canal, the frequency-dependent velocity profile exists in two distinct shapes, one in phase with the motion of the duct and the other out of phase. This unsteady effect, elicited here by harmonic motion of the duct wall, is similar to that studied by Womersley (1955, 1958) for an internal flow induced by imposing a harmonically varying pressure gradient. When the unsteady forces are small relative to the viscous forces, the velocity profile assumes an almost parabolic distribution which minimizes the viscous drag between the endolymph and the duct wall. As the unsteady forces increase, the velocity profile becomes more complicated (see figure 7) with an increased slope and greater viscous drag at the wall. This unsteady effect, which influences the shape of the velocity profile, depends on the volumetric flow rate and the geometry of the duct (both in terms of the size and shape of the cross-sectional area). It is accounted for in Δp_v^* by the frequency-dependent viscous-shear-stress factor, λ (see figure 3), which determines, from the shape of the velocity profile, the magnitude and phase of the shear stress at the wall relative to the dimensionless volumetric flow rate. In the long-and-slender portion of the duct, the velocity profile is almost identical to a steady Poiseuille flow over the entire range of physiological frequencies and thus the unsteady effects do not play a significant role there. It is only in the utricle and ampulla, where the cross-sectional area is large, that the unsteady out-of-phase component becomes important.

The aforementioned mass and viscous terms account for the effective loading of the entire loop of endolymph in the outer region on the cupula. These terms do not, however, address local mass entrainment by the cupula or viscous dissipation. In deriving these terms, spatial dependence was integrated out of the cupular deformation field. The boundary-layer term, Δp_b^*, accounts for the combined mass and viscous effect associated with the local multi-dimensional fluid dynamics within the ampulla. Owing to the viscoelasticity of the cupula and the enlarged ampullary radius, the velocity profile of the endolymph on the surface of the cupula undergoes a significant change in shape from the high-Stokes-number flow in the ampulla, through the boundary layer, to the simpler profile in the outer region. In this transitional region, the viscous forces associated with changes induced in the velocity profile introduce mode coupling into the vibrational shapes of the cupula. This local viscous drag in the ampullary boundary layer is accounted for by Δp_b^* which represents the cumulative effect, over the entire length of the boundary layer, of the viscous pressure loss associated with the change in shape the velocity profile experiences through the transitional region. In addition to the viscous effect, the fluid dynamics in the ampullary boundary layer causes an entrainment of endolymph by the cupula. The entrained endolymph, which follows the pointwise displacement of the cupula, results in a local mass loading effect. The amount of entrained mass correlates with the thickness of the boundary layer (see figure 6). In addition, the boundary-layer thickness is also related to

the local viscous drag in the ampulla. At low frequencies the fluid dynamics in the ampulla corresponds to a low-Stokes-number flow resulting in a Poiseuille-like cupular displacement profile. Under these circumstances the boundary-layer thickness is large resulting in little viscous dissipation through the transitional region (in fact, at frequencies below 1 Hz there is essentially no transitional-flow region). At higher frequencies the unsteady fluid dynamics plays a greater role and the boundary-layer thickness decreases resulting in greater viscous action required to change the shape from the complicated velocity profile at the surface of the cupula to the simpler low-Stokes-number profile in the outer region.

Since the outer-region solution cannot address the spatial distribution of the cupular deformation field, it is necessary to include Δp_b^* in order to quantify the multi-dimensional fluid dynamics within and ampulla, its interaction with the cupula, and the relationship between the micromechanical deformation field of the cupula and the afferent response measured within the vestibular nerve. Specific numerical results applying all four terms are provided for the geometry of the toadfish horizontal canal using a simple axisymmetric model of the cupula. In the discussion which follows, we consider (i) the spatially averaged response dynamics predicted by the outer-region solution, (ii) the fluid dynamics within the ampulla in the absence of any fluid–structure interaction with the cupula, (iii) the influence of the cupula on the micromechanics and its response sensitivity to changes in cupular parameters, and (iv) how the micromechanics predicted here, for this simple axisymmetric model of the cupula, correlates to the afferent response measured within the vestibular nerve.

7.2. *Spatially averaged displacement and pressure*

Consistent with previous models, the velocity-proportional deflection of the cupula evident in the middle-frequency range arises owing to a balance between the viscous drag and inertial forcing of the endolymph (see figure 4). At frequencies below 0.1 Hz, the system becomes dominated by the stiffness of the cupula resulting in a decrease in the average displacement gain and an increase in the phase. Since the cupular stiffness, T, and viscosity, ν_p, represent the most uncertain parameters utilized in the current numerical examples, the effect of varying these parameters is considered throughout. For a cupular stiffness below 0.35 dyn cm^{-1} the average displacement gain and phase remain approximately flat between 0.01 and 10 Hz with the average displacement of the cupula aligning approximately with the velocity of the head. Below 0.01 Hz the phase is seen to increase while the gain is seen to decrease with a corner frequency occurring near 0.01 Hz. A smaller stiffness results in a lower corner frequency. Also consistent with previous models, the spatially averaged gain is seen to decrease at high frequencies above 10 Hz accompanied with a decrease in phase as a result of endolymphatic mass loading acting on the cupula.

For the present model geometry, a simple torsion-pendulum model predicts the mass cutoff at an upper-corner frequency of about 53 Hz which is higher than the present prediction of 20 Hz. This discrepancy is due to the relative size of the coefficients of the mass and viscous terms. Owing to the inverse area dependence appearing in the mass coefficient, the endolymph contributes more to the effective mass loading on the cupula in regions of small cross-sectional area than it does in the utricle where the cross-section is large. This is true to a greater extent for the viscous loading on the cupula owing to the inverse-square area dependence in the viscous coefficient. In the torsion-pendulum model, the mass and viscous coefficients are both over-estimated if they are computed for a toroid having a uniform cross-sectional area based on the slender portion of the duct. The fast time constant is given by the ratio of the

mass to viscous coefficients and is responsible for the location of the high-frequency cutoff in the gain. Thus, simple torsion-pendulum models typically over-estimate the viscous coefficient to a greater extent than the mass coefficient which results in underestimating the fast time constant. This in turn causes the corner frequency to occur higher in the frequency spectrum than is predicted by more descriptive models (Oman *et al.* 1987; Rabbitt & Damiano 1992). Nevertheless, both models predict a cutoff in the spatially averaged displacement gain at high frequencies. The spatially averaged gain and phase remain qualitatively unchanged as the viscosity of the cupula is varied. Substantially increasing the viscosity of the cupula only slightly lowers and widens the plateau of the spatially averaged displacement gain and leaves the phase relatively unchanged.

The spatially averaged transcupular pressure monotonically increases as function of frequency and exhibits sensitivity to the stiffness and viscosity of the cupula. However, whereas the phase of the average displacement is relatively insensitive to the viscosity of the cupula, the phase of the pressure is not. This can be seen by comparing panels (*b*) and (*d*) in figure 4. Results show that, while the average displacement of the cupula and the differential pressure are both sensitive to the macromechanical fluid dynamics, the pressure is far more sensitive to the properties of the cupula.

The parameter sets represented in figure 4 include the case where the cupular stiffness, T, is taken to be 0.35 dyn cm^{-1} since this value reflects the same lower corner frequency as is seen in the afferent data of the toadfish reported by Boyle & Highstein (1990). The stiffness that reproduces the lower corner frequency is considered an upper bound since adaptation mechanisms would only further increase the corner frequency. Considering progressively softer cases, each differing by an order of magnitude, helps illustrate a limiting trend as the stiffness goes to zero. In passing to this limit, the elastic restoring force is forfeited and the cupular model approaches a linearly viscous fluid. Such a limit is useful in § 7.3 as we investigate the multi-dimensional fluid dynamics in the ampulla. Assuming that the viscosity of the cupula, ν_p, is bounded below by that of the endolymph, the case corresponding to $\nu_p = 0.0085$ cm^2 s^{-1} was included in figure 4, which is the value reported for the kinematic viscosity of endolymph by Steer *et al.* (1967). The larger value of the cupular viscosity shown for the case where $\nu_p = 29.0$ cm^2 s^{-1} (with a corresponding dynamic viscosity of 29.0 P) is an estimate taken from Rabbitt *et al.* (1994). Relatively large viscosities such as this are not uncommon in biological materials. For example, the gross dynamic viscosity of cytoplasm was reported as being 130 P in neutrophils (Schmid-Schönbein *et al.* 1981) and ranged from 0.097 to 0.28 P in red blood cells (Sutera, Mueller & Zahalak 1990). The apparent sensitivity to cupular viscosity is notable.

For comparison, panels (*e*) and (*f*) of figure 4 show the gain and phase of afferents from the toadfish horizontal canal nerve (Boyle & Highstein 1990). Within the afferent population, the variation in the response dynamics between individual afferent units is marked and continuously distributed. Boyle & Highstein (1990) grouped the afferents according to their response dynamics into three broad classes as reproduced here (low-gain, LG; high-gain, HG; and acceleration A). It is interesting that the dynamics of LG class afferents correlate well with the spatially averaged displacement of the cupula, and the response dynamics of A type units correlate with the macromechanics of the transcupular pressure. (Rabbitt *et al.* 1994).

Since the analysis is linear, spatially averaged results obtained when ignoring the boundary layer (i.e. the outer-region solution taken alone) cannot be distinguished from the results shown in figure 4 for the full problem. This is due to the fact that

the boundary-layer pressure variation across the surface of the cupula averages to zero when taken over the entire cross-section. It is only when we address the spatial distribution of cupular deflection or transcupular pressure that the boundary layer becomes important.

7.3. *Fluid dynamics within the ampulla*

The analysis addresses the unsteady fluid dynamics within the endolymphatic duct during sinusoidal oscillation of the head. Two important dimensionless groups which arise are the Stokes number (which characterizes the ratio of unsteady inertial forces to viscous forces) and the Reynolds number (which characterizes the ratio of steady inertial forces to viscous forces). In the long-and-slender portion of the duct, the characteristic Stokes number (based on the characteristic cross-sectional radius of the duct) varies from 2.7×10^{-4} to 27 over the frequencies ranging from 0.001 Hz to 100 Hz.† The ampullary Stokes number (based on the radius of the ampulla at the cupula) is larger by approximately a factor of 22. Over this same frequency range, the Reynolds number associated with the long-and-slender region of the duct varies from 5.4×10^{-5} at 0.001 Hz to 5.4 at 100 Hz for a 1° peak-to-peak angular head amplitude. It should be pointed out that the Reynolds number used in our analysis is based on the characteristic velocity of the duct wall and not on the fluid velocity relative to the duct wall. The characteristic velocity U of the duct wall varies from 2.4×10^{-5} cm s^{-1} at 0.001 Hz to 2.4 cm s^{-1} at 100 Hz. If we compute a Reynolds number based on the average velocity of endolymph relative to the duct wall we find the *relative* Reynolds number varies from 1.5×10^{-11} at 0.001 Hz to 0.4 at 100 Hz. This shows that the average velocity of endolymph relative to the duct wall is more than 6 orders of magnitude smaller than the characteristic velocity at 0.001 Hz and more than 1 order of magnitude smaller at 100 Hz. Thus, the *relative* Reynolds number remains less than 1 over the entire physiological frequency spectrum resulting in a viscously dominated laminar flow within the long-and-slender portion of the duct. In the ampulla, these Reynolds numbers are larger by approximately a factor of 5.

Owing to the long-and-slender toroidal geometry and the relatively low frequencies associated with physiological rotation of the head, the fluid dynamics in the slender regions of the canal corresponds to a Stokes number much less than 1 such that steady viscous effects dominate. As a result, the endolymphatic fluid dynamics in the long-and-slender duct is essentially characterized by a slowly oscillating Poiseuille flow. In the utricle and in the ampulla the cross-sectional area is sufficiently large such that unsteady cross-sectional modes play an important role, especially at high physiological frequencies of head rotation. We address this directly in the outer part of the asymptotic expansion by including the influence of the Stokes number on the magnitude and phase of the spatially distributed viscous drag force.

Of greatest significance is the multi-dimensional fluid–structure interaction within the ampulla and its impact on the deflected shape of the cupula. Results show that the local deflection is not a simple reflection of the spatially averaged cupular displacement and hence the mechanical stimuli activating transduction are not simply proportional to the 'global' cupular deflection (see figures 5 and 8). This applies to both the gain and phase of the mechanical response and is significant at frequencies above approximately 0.3 Hz in the toadfish (the exact frequency is sensitive to the

† The physiological-frequency range is usually defined below 10 Hz in experimental studies. Theoretical results presented here are extended to 100 Hz based on recent experimental data showing that canal afferents respond to high frequencies of mechanical stimulation (Rabbitt *et al.* 1995*b*).

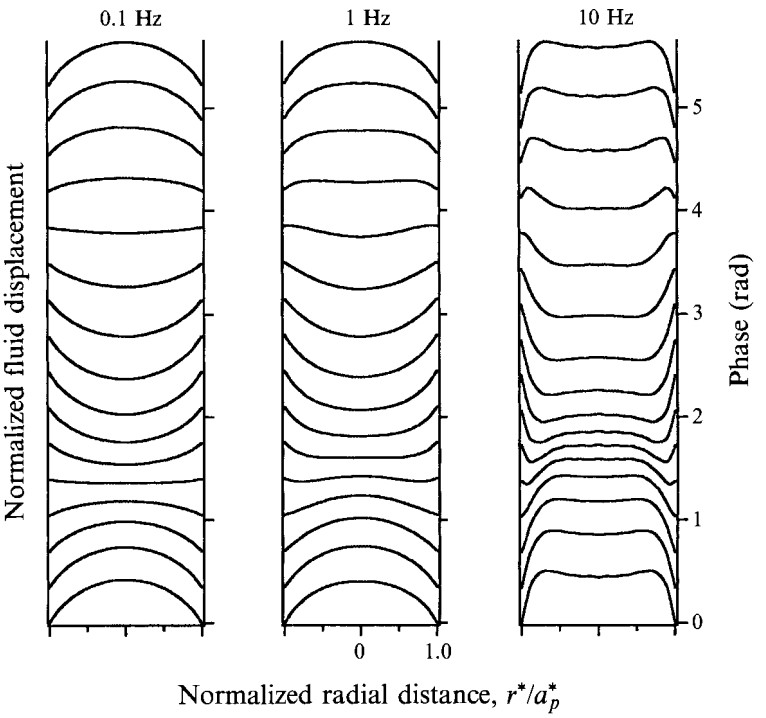

FIGURE 7. The fluid displacement profiles of the endolymph in the ampulla in the absence of the cupula are shown here over one cycle at 0.1, 1, and 10 Hz (with corresponding ampullary Stokes numbers of 0.6, 6, and 60, respectively where $a_p^* = 0.09$ cm). At 0.1 Hz we see an essentially parabolic Poiseuille flow distribution. As the frequency increases above 1 Hz, the displacement gradient begins to steepen at the wall producing an almost slug-like flow at 10 Hz. The profiles shown here correspond to the case in which the cupular density and viscosity are equal to that of the endolymph and the membrane thickness and stiffness vanish. This choice of parameters results in the cupula imitating the endolymph and therefore gives the fluid displacement profiles as they would appear in the absence of the cupula.

mechanical properties of the cupula). Since the gross morphology of the semicircular canals and the range of physiological frequencies in primates is similar to the toadfish, a difference between the local response and the spatially averaged response is expected to apply to other species as well. For example, Damiano (1993) provides results of the boundary-layer analysis for the human geometry which exhibit a similar deviation in the local response from the spatially averaged response.

The enlargement of the canal at the ampulla contributes to the local/global disparity in two ways. First, the diameter of the ampulla is large enough that the local ampullary Stokes number exceeds 20 in the physiological frequency range (see figure 6). Because of this, even in the absence of the cupula, the endolymph does not acquire a Poiseuille profile in the ampulla as it does in the canal duct, but rather takes on a phase-dependent unsteady distribution. At these higher frequencies, the slope of the velocity profile at the wall, which reflects the cupular shear and associated stereocilia deflection, deviates substantially from the Poiseuille slope in both magnitude and phase (see figure 7).

To illustrate the influence of the Stokes number on the ampullary flow, we present the case in which the density and viscosity of the cupula are identical to the endolymph and the stiffness is set to zero. In passing to this limit, the cupula, as we have modelled

it (see the Appendix), becomes a slice of fluid equivalent to endolymph which fills a cross-section of the ampulla. Ampullary endolymphatic displacement profiles are shown for this case in figure 7 over one cycle at frequencies of 0.1 (left), 1 (centre), and 10 Hz (right). A frequency of 10 Hz corresponds to a Stokes number of 60 resulting in a more complicated slug-like displacement profile with a relatively steep slope at the wall as compared with the simpler Poiseuille-like profile which exists at 0.1 Hz.

The natural tendency of the fluid to acquire a more complex velocity distribution at high frequencies is compounded by a second effect of the enlarged ampulla – the enlargement increases the mobility of the cupula. Without the enlargement, interfacial molecular tension alone (existing between the cupula and the endolymph) could completely dominate the mechanical stiffness and substantially attenuate the macromechanical response. The increased mobility of the cupula, coupled with the stiffness of this structure, results in a more complicated interaction with the endolymph than occurs in the case when the cupula is absent as shown in figure 7. The implications of cupular stiffness and viscosity on the fluid dynamics are discussed below.

7.4. *Contributions of the cupula*

Even for the highly simplified cupular model employed here, the local response of the cupula is much more sensitive to model parameters than the spatially averaged response. For example, the angular shear of the cupula computed at the surface of the crista shows sensitivity to the cupular stiffness in the high physiological frequency range but the average cupular deflection is completely insensitive to the stiffness over this same range (see figures 4 and 5). This is true even for the simple axisymmetric homogeneous viscoelastic membrane model of the cupula. Given the geometry, inhomogeneity, and anisotropy of the actual cupula, we would expect it to exhibit even more spatial diversity in the local deflection field than this simple model predicts. These observations provide theoretical evidence that the mechanical deflection of the stereocilia, elicited by the semicircular canal mechanics, deviates from predictions of all two-time-constant models and all torsion-pendulum-type models in the high-frequency range. Since results show sensitivity to the cupular stiffness and viscosity, which are as yet unknown parameters, and since we have not included the ultrastructure or asymmetry of the cupula, we do not expect the high-frequency shear angle of the example results to reflect the actual angular deflection of the cupula. Nevertheless, results clearly show the impact of the ampullary boundary layer on the response and provide a straightforward means to include it in future models of cupular dynamics. Furthermore, for a physiological stimulus, the response dynamics shown in figure 5 result in amplitudes of the angular displacements of stereocilia that are within the physiological range based on the response of isolated hair cells elicited by stereocilia deflections (Hudspeth & Jacobs 1979; Corey & Hudspeth 1983; Fettiplace, Crawford & Evans 1992).

We stress that the ampullary boundary layer (Δp_b^* given by (1.5)) has almost no influence on the spatially averaged macromechanical endolymphatic flow or pressure, but influences the local cupular deformation field significantly. Previous models ignoring the boundary layer are not adequate to address the pointwise displacement of the cupula (see Damiano 1993 for more details). For a large cupular stiffness, such as the value which produces a lower corner frequency at 0.03 Hz, the ampullary boundary layer does not completely eliminate structural modes of vibration of the cupula. It is only when the cupula is very soft that the boundary layer dominates

and eliminates the structural modes of the cupula. If the stiffness of the cupula is selected to reproduce the average lower-corner frequency measured within the afferent nerve and the viscosity is low (equal to that of endolymph), then very low quality mechanical resonances are observed in the local deflection of the cupula at discrete frequencies. It is also possible that slow components of adaptation, such as associated with the transduction current (Assad & Corey 1992; Eatock, Corey & Hudspeth 1987; Highstein, Rabbitt & Boyle 1995), may contribute to the lower corner frequency. If adaptation is significant in shaping the lower corner then the lower values of stiffness shown in the example results may be the most physiologically relevant. Adequate experimental data are not currently available to resolve this ambiguity between the cupular stiffness and adaptation.

Semicircular-canal hair-cell stereocilia can reach 100 microns in total length. This is substantially longer than stereocilia from otolithic or cochlear organs, but still represents only 5% of the distance across the ampulla. The cupular profiles shown in figure 8 indicate that the angular displacement along the length of a stereociliary bundle is relatively homogeneous. Although the distribution of deflection along the length of semicircular-canal stereocilia has not been measured to date, the present theoretical results suggest that the angular deflection along individual bundles is relatively uniform and that the angular deflection at the surface of the sensory epithelium is a reasonable measure of the mechanical activation. Complicating this apparent homogeneity in microdomain cupular shear angle, it is possible that some differential motion exists between the cupula and the embedded stereociliary bundles. Hence it is important to note that the motion of the cupula may not directly determine the nanomechanical motion of individual stereocilia or the associated transduction channel gating. In this sense, the angular deflection of the cupula at the surface of the sensory epithelium is recognized as a determinant of stereociliary bundle displacement and is not equal to bundle displacement itself. The present results do not address this difference. The present microdomain results simply apply to the 'shear angle' of a simple model cupula at the surface of the sensory epithelium.

Whereas the spatially averaged displacement of the cupula is relatively insensitive to the broad range of cupular viscosities considered, the microdomain shear angle is not. Cupular viscosity introduces damping into the local displacement field of the cupula which results in dissipative mode coupling much in the same way that the boundary layer influences the local displacement field of the cupula. For the larger cupular viscosities shown in figure 5, the high-frequency shear-angle gain and phase enhancements which arise owing to the multi-dimensional fluid dynamics in the ampulla are overwhelmed by the viscous effects of the cupula. For cupular viscosities several orders of magnitude greater than the viscosity of endolymph, we find that the local response dynamics at the cupula–crista interface is qualitatively indistinguishable from the spatially averaged displacement shown in figure 4.

The sensitivity of the shear-angle gain to the stiffness of the cupula is shown in figure 5. Perhaps the most significant influence of the stiffness can be seen by comparing the displacement profiles at 10 Hz in figures 7 and 8. Whereas the fluid displacement profile in the absence of the cupula assumes an almost slug-like flow at 10 Hz (see figure 7), the presence of the elastic restoring force of a membranous structure results in the more complicated profiles at 10 Hz shown in figure 8. Displacement profiles are shown at several frequencies with a membrane stiffness of 0.035 dyn cm^{-1} and a density and viscosity equal to that of the endolymph. For the three frequencies shown, the corresponding Stokes numbers are the same as

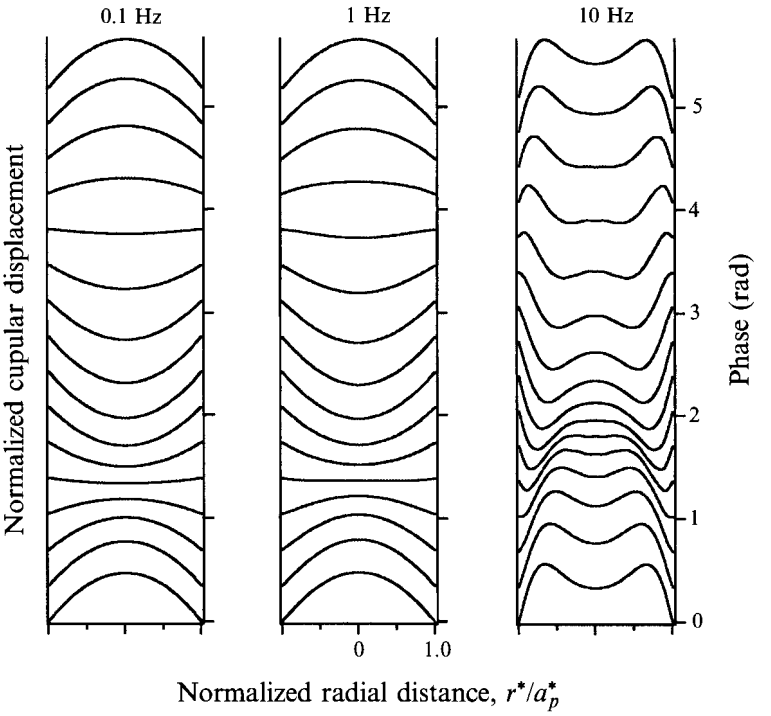

FIGURE 8. The displacement profiles of the cupula are shown here over one cycle at 0.1, 1, and 10 Hz. Notice the effect that the membrane stiffness has on the shape of the profile at 10 Hz compared with the shape that the fluid profile would assume in the absence of the cupula (see figure 7). The profiles shown here correspond to a cupular stiffness of 0.035 dyn cm^{-1} and a density and viscosity which is equal to that of the endolymph. For displacement amplitudes, refer to figure 5.

those given for the displacement profiles of the endolymph shown in figure 7. The important distinction to notice between the displacement profiles with and without the cupula is the influence of cupular stiffness. The restoring force that the cupula exerts on the fluid serves to constrain the fluid to move with the cupula which in turn retards steepening of the displacement gradient at the wall for Stokes numbers greater than 1.

Frequency-dependent cross-sectional pressure distributions acting over the surface leaflets of the cupula are shown in figure 9. The pressure fields were computed by subtracting the instantaneous outer-region pressure (i.e. $\Delta p_i^* - \Delta p_m^* - \Delta p_v^*$, which is constant over the cross-section at any instant in time) from the overall pressure differential Δp^* across the cupula predicted by the combined theory given by (1.1). Figure 9 shows the time development of the spatially dependent term in (3.45), or Δp_b^* given in dimensional form by (1.5). It is interesting to note the magnitude of the cross-sectional variations in the differential pressure predicted by the boundary-layer solution compared with the instantaneous macromechanical differential pressure predicted by the outer-region solution alone. For example, for the profiles shown in figure 9, at 1 Hz the outer-region solution predicts a macromechanical transcupular differential pressure of 0.78 dyn cm^{-2} (for a zero-to-peak angular head amplitude of 1 radian). According to the current theory, in certain locations in the cross-sectional distribution field, the spatial variability in pressure is predicted to be as much as 25% that of the macromechanical value (at 1 Hz this occurs near the centre of the duct

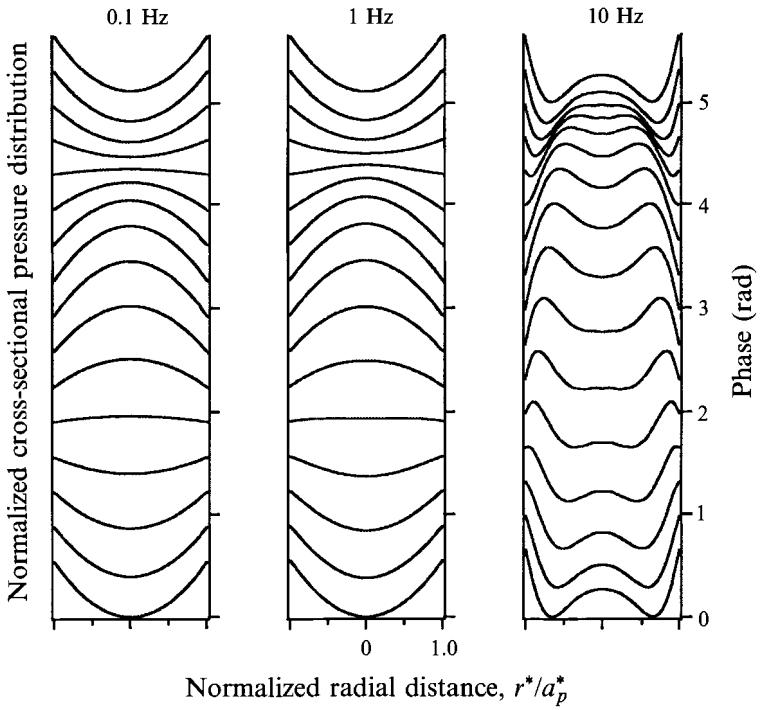

FIGURE 9. Shown here are the pressure distribution profiles in the ampullary boundary layer acting over the surface leaflets of the cupula which correspond to the displacement profiles shown in figure 8. The pressure profiles are computed by subtracting off the time-dependent outer-region solution which is uniform over the cross-section. This corresponds to the second term in (3.45) or Δp_b^* given by (1.5) which represents the spatially distributed difference in the instantaneous pressure field predicted by the boundary-layer and outer-region solutions. Notice again, the parabolic distribution in the profiles at 0.1 Hz as compared with the more complicated flow distribution which appears at 10 Hz.

— see figure 9). At 10 Hz, the maximum spatial variability is almost 18% of the macromechanical value.

The simple model of the cupula was presented primarily to illustrate the behaviour of the ampullary boundary layer and we have made no attempt to optimize cupular parameters. Nevertheless, it is interesting to compare the magnitude of the stiffnesses shown in figures 4 and 5 to other values of stiffness appearing in biological materials. For example, the passive cortical tension in the membrane of granulocytes was reported by Evans & Dembo (1990) to be 0.035 dyn cm^{-1} which coincidentally is the same as the value chosen for the membrane tension corresponding to displacement and pressure profiles shown in figures 8 and 9. It is not clear whether the cupular restoring force is better modelled with bending elasticity rather than membrane prestress. In a bending mode, a stiffness of 4.7×10^{-5} dyn cm^{-1} reproduces the same macromechanical response as is shown in figure 4 for a corresponding membrane stiffness of 0.035 dyn cm^{-1}. A comparison of the cupular shear angle shows that the local micromechanics is qualitatively similar with both types of restoring-force mechanisms showing the characteristic high-frequency gain and phase enhancement seen in figure 5 (in the case of bending stiffness, this enhancement occurs slightly higher in the frequency spectrum). Assuming the cupular material to be incompressible (with Poisson's ratio equal to 1/2) a bending stiffness of 4.7×10^{-5} dyn cm^{-1} and a thickness

of 0.05 cm corresponds to an extensional Young's modulus of 3.4 dyn cm^{-2}. To put this in perspective, this is substantially lower than the stiffness of 275 dyn cm^{-2} reported by Schmid-Schönbein *et al.* (1981) for the cytoplasm of neutrophils and nearly equal to the dynamic stiffness of respiratory tract mucus (Lutz, Lutt & Chakrin 1973)

7.5. *Relationship to the afferent response*

The first-order afferent response depends on many factors. One among these is the macromechanics of endolymph flow and pressure. Other factors which influence the response dynamics of the afferent nerve include the micromechanical response of the cupula and the deflection of individual cilia, mechanotransduction in hair cells, processing by hair-cell currents, the dynamics associated with the activation of vesicle binding and release of neurotransmitter, and post-synaptic binding and summation (Guyton 1986; Hudspeth 1983). A motivating factor in this paper has been the degree to which the mechanics has bearing on the afferent response and the extent to which it may account for the variation among the afferent units within the vestibular nerve. The variation within the afferent population was discussed earlier in relation to figure 4. While the source of this variation is not yet completely understood, explanations involve processing by hair-cell/afferent complexes and the non-uniform spatial variations in the displacement field of the cupula (Highstein *et al.* 1995; Honrubia *et al.* 1989; Boyle *et al.* 1991; Goldberg *et al.* 1992; Hillman 1974; McLaren & Hillman 1979). The present biomechanical results are most consistent with electrophysiological results provided by Highstein *et al.* (1995) describing responses of individual afferents in terms of a combination of mechanical and post-transduction signal processing. They attribute less than half of the diversity observed across the population of afferents to the mechanics. Even though the cupula model employed in the present study is quite limited, numerical results show spatio-temporal inhomogeneity consistent with the hypothesis that local variations in the deformation of the cupula contribute to the diversity of afferent responses.

8. Summary and conclusions

A mathematical analysis is presented that describes the fluid–structure interaction which takes place within the ampulla of the vestibular canal. Using a singular perturbation method and a matched asymptotic analysis, the model details the two-dimensional axisymmetric velocity field in a boundary-layer region surrounding the cupula. The governing equations were linearized for small perturbations in fluid displacement around the prescribed motion of the endolymphatic duct wall. The new boundary-layer model was solved analytically and combined with previous results for the outer region to relate the differential pressure drop through the boundary layer to the pointwise deflection of the cupula. The analysis leads to a relatively simple expression for the transcupular pressure field in terms of the prescribed motion of the head, morphology of the semicircular canal duct, and motion of the cupula. This result provides a dynamical boundary condition acting on the surfaces of the cupula and represents the primary contribution of the present work.

As an example of how to use the new mathematical result, the boundary condition was coupled to a simple viscoelastic model of the cupula and applied to the semicircular canal geometry of the toadfish, *Opsanus tau*. The spatially averaged displacement field of the cupula (macromechanics) showed the same response as previous macromechanical models of canal dynamics (Oman *et al.* 1987; Van Buskirk *et*

al. 1976; Van Buskirk 1987). However, the pointwise displacement of the cupula and the shear strain acting on the stereociliary bundles differ significantly from macromechanical models. For a cupular stiffness between 0.0035 and 0.035 dyn cm^{-1} and a cupular viscosity equal to that of endolymph, the cupular-shear-angle gain, defined by the slope of the cupula at the wall divided by the angular velocity of the head, was relatively constant and equal to $9.2 \times 10^{-3\,\circ}(^{\circ}s^{-1})^{-1}$ over the range of frequencies from 0.01 Hz up to about 1 Hz. Over this same range, the phase was approximately zero. Above 1 Hz, the cupular-shear-angle gain increased slightly while the phase showed a lead of as much as 30°. High-frequency increases in gain and phase exist locally on the cupula but are absent in the spatially averaged macromechanical deflection.

Results show that the spatio-temporal response of the cupula is sensitive to the multi-dimensional interaction of the cupula with the surrounding ampullary endolymph. Various regions of the cupula are coupled together via the endolymph in the boundary layer. This local coupling has a strong influence on the pointwise deflected shape of the cupula and hence is important in determining the mechanical stimulus activating sensory hair-cells. Comparison of the theoretical results of the model to the afferent data recorded from the vestibular nerve suggests that the local micromechanics may account for some of the observed high-frequency gain and phase enhancement but cannot alone account for the broad range of responses elicited among the afferent population.

Sensitivity of the local deflection field to cupular material parameters strongly indicates that current models of the cupula are inadequate and probably do not capture the spatial distribution of cupular deflection. In future work, appropriate constitutive models must be determined experimentally in order to properly describe and model the mechanical behaviour of the cupula. A morphologically accurate geometrical model of the cupula and realistic boundary conditions at the cupula–crista interface must also be established. Direct experimental measurements of the cupula deflection field will also be necessary to validate any modelling efforts. This may be particularly relevant when attempting to address metabolically active motile mechanisms that may be playing a role in cupular dynamics (Rüsch & Thurm 1990). Although some evidence suggests that the role of active motility may be small compared to passive mechanics (Highstein *et al.* 1995), it cannot be ruled out as a possible contributor to local-domain cupular dynamics. These topics remain the subject of future investigations.

The authors gratefully acknowledge Dr Mark Holmes for his valuable contributions during the development of the mathematical analysis. Partial support for this work was contributed by the National Institutes of Health, NIDCD 5P01 DC01837, and the National Science Foundation, BCS-8957206.

Appendix. Momentum equation for the cupula

The asymptotic analysis carried out here is specifically designed to lump the influence of the entire endolymphatic fluid dynamics into a dynamic boundary condition acting on the leaflet surfaces of the cupula. The result provides a relationship between the pressure differential acting across the cupula, the acceleration of the head, and the velocity and acceleration of the cupula itself. This expression is coupled to the cupula using the momentum equation governing the displacement of the cupula. Treating the cupula as a simple material continuum as described in § 4, the momentum equation

has the form

$$\mathbf{L}^*[\boldsymbol{w}^*] = (p_2^* - p_1^*)\boldsymbol{n}_p, \tag{A 1}$$

where $\boldsymbol{w}^*$ is the three-dimensional deformation field of the cupula in dimensional units, $\mathbf{L}^*$ is a matrix of differential operators, p_2^* and p_1^* are the dimensional pressures acting on the surfaces of the cupula, and $\boldsymbol{n}_p$ is the outward unit normal vector to the surface of the cupula leaflets. Regardless of the specific constitutive behaviour of the cupula, the expression for the endolymph pressure provides the forcing in this equation.

We treat the cupula as two linearly elastic membranes retaining a passive linearly viscous fluid. This assumption does not restrict the validity or application of the matched asymptotic expansion for the fluid dynamics and is presented here primarily as an example. The dimensionless transverse displacement of the cupula, $w_s = \omega w_s^*/U$, is expanded in a series in terms of ε such that $w_s = w_{s_0} + \varepsilon w_{s_1} + \cdots$. In a similar manner as with the fluid, a new variable, w, is defined which represents the displacement of the cupula relative to the duct wall such that the boundary conditions are homogeneous. To leading order, the equation of motion and boundary condition governing the transverse displacement of the cupula, w_0, relative to the duct wall are given by

$$\frac{St}{Re}\frac{\partial^2 w_0}{\partial t^2} - \frac{\nu_p/\nu}{Re}\nabla_c^2\left(\frac{\partial w_0}{\partial t}\right) - \nabla_c \cdot (\psi \nabla_c w_0) = -\frac{St}{Re}R_p\ddot{\Omega} + \frac{1}{2}\frac{\rho/\rho_p}{h/l}\Delta p_0, \tag{A 2}$$

and

$$w_0|_\sigma = 0, \tag{A 3}$$

where σ is the curve which corresponds to the boundary of the cupula partition and ψ is the dimensionless stiffness of the cupula given by

$$\psi = \frac{T}{\rho_p h a_0 \omega U}. \tag{A 4}$$

Here ν_p is the kinematic viscosity of the cupular fluid, ρ_p and h are the density and thickness of the cupula, respectively, and T is the membrane tension of the cupula at equilibrium. The dimensionless stiffness, ψ, may in general depend on r and φ since both the stiffness, T, and thickness, h, may vary over the cross-section. The pressure appearing in this equation is replaced by the asymptotically determined fluid pressure to obtain the numerical results presented herein.

Note, if we consider a degenerate case when the stiffness, T, vanishes and the viscosity and density of the cupula are equal to that of the endolymph, then, in passing to the limit as the dimensionless length h/l tends toward zero, we retrieve the $O(1)$ equation governing the fluid given by (2.12). Notice that

$$\lim_{h/l \to 0} \frac{\Delta p_0}{h/l} = -\frac{\partial p_0}{\partial s}. \tag{A 5}$$

REFERENCES

ASSAD, J. A. & COREY, D. P. 1992 An active motor model for adaptation by vertebrate hair cells. *J. Neurosci.* **12**, 3291–3309.

BLANKS, R. H. I., ESTES, M. S. & MARKHAM, C. H. 1975 Physiologic characteristics of vestibular first-order canal neurons in the cat. II. *J. Neurophysiol.* **38**, 1250–1268.

BOYLE, R., CAREY, J. P. & HIGHSTEIN, S. M. 1991 Morphological correlates of response dynamics and efferent stimulation in horizontal semicircular canal afferents of the toadfish, *Opsanus tau*. *J. Neurophysiol.* **66**, 1504–1521.

BOYLE, R. & HIGHSTEIN, S. M. 1990 Resting discharge and response dynamics of horizontal semicircular canal afferents of the toadfish, *Opsanus tau. J. Neurosci.* **10**, 1557–1569.

COREY, D. P. & HUDSPETH, A. J. 1979 Ionic basis of the receptor potential in a vertebrate hair cell. *Nature* **281**, 675–677.

COREY, D. P. & HUDSPETH, A. J. 1983 Kinetics of the receptor current in bullfrog saccular hair cells. *J. Neurosci.* **3**, 962–976.

CRUM-BROWN, A. 1874 On the sense of rotation and the anatomy and physiology of the semicircular canals of the inner ear. *J. Anat. Physiol.* **8**, 327–331.

CURTHOYS, I. S. & OMAN, C. M. 1987 Dimensions of the horizontal semicircular duct, ampulla and utricle in the human. *Acta Otolaryngol. (Stockh.)* **103**, 254–261.

DAMIANO, E. R. 1993 Continuum models of rotational and caloric stimulation of the vestibular semicircular canal. PhD thesis, Rensselaer Polytechnic Institute, Troy, NY.

EATOCK, R. A., COREY, D. P. & HUDSPETH, A. J. 1987 Adaptation of mechano-electrical transduction in hair cells of the Bullfrog's sacculus. *J. Neurosci.* **7**, 2821–2836.

EVANS, E. & DEMBO, M. 1990 Physical model for phagocyte motility: Local growth of a contractile network from a passive body. In *Biomechanics of Active Movement and Deformation of Cells* (ed. N. Akkas), NATO ASI Series, vol. H42, pp. 185–214. Springer.

EWALD, J. R. 1887 Zur physiologie der bogengänge. *Pflügers Arch. Ges. Physiol.* **41**, 463–483.

FERNÁNDEZ, C. & GOLDBERG, J. M. 1971 Physiology of peripheral neurons innervating semicircular canals of the squirrel monkey. II Response to sinusoidal stimulation and dynamics of peripheral vestibular system. *J. Neurophysiol.* **34**, 661–675.

FETTIPLACE, R., CRAWFORD, A. C. & EVANS, M. G. 1992 The hair cell's mechanoelectrical transducer channel. *Ann. NY Acad. Sci.* **656**, 1–11.

GOLDBERG, J. M. & FERNÁNDEZ, C. 1971 Physiology of peripheral neurons innervating semicircular canals of the squirrel monkey. III Variations among units in their discharge properties. *J. Neurophysiol.* **34**, 676–684.

GOLDBERG, J. M., LYSAKOWSKI, A. & FERNÁNDEZ, C. 1992 Structure and function of vestibular nerve fibers in the chinchilla and squirrel monkey. *Ann. NY Acad. Sci.* **656**, 92–110.

GROEN, J. J. 1949 *Medische Physica; de Evenwichtszintuigen*, pp. 510–561. Amsterdam: NH Uitgeversmij.

GROEN, J. J. 1957 The mechanics of the semicircular canals. *J. Physiol. Lond.* **110**, 1–17.

GUYTON, A. C. 1986 *Textbook of Medical Physiology*. W. B. Saunders Company, Philadelphia, PA.

HARTMANN, R. & KLINKE, R. 1980 Discharge properties of afferent fibers of the goldfish semicircular canal with high frequency stimulation. *Pflügers Arch.* **388**, 111–121.

HIGHSTEIN, S. M., RABBITT, R. D. & BOYLE, R. 1995 Determinants of semicircular canal response dynamics in the toadfish, *Opsanus tau. J. Neurophysiol.* (in press).

HILLMAN, D. E. 1974 Cupular structure and its receptor relationship. *Brain Behav. Evol.* **10**, 52–68.

HONRUBIA, V., HOFFMAN, L. F., SITKO, S. & SCHWARTZ, I. R. 1989 Anatomic and physiologic correlates in bullfrog vestibular nerve. *J. Neurophysiol.* **61**, 688–701.

HUDSPETH, A. J. 1983 Mechanoelectrical transduction by hair cells in the acousticolateralis sensory system. *Ann. Rev. Neurosci.* **6**, 187–215.

HUDSPETH, A. J. & JACOBS, R. 1979 Stereocilia mediate transduction in vertebrate hair cells. *Proc. Natl Acad. Sci. USA* **76**, 1506–1509.

IGARASHI, M. 1966 Dimensional study of the vestibular end organ apparatus. *Second Symp. on the Role of Vestibular Organs in Space Exploration.* NASA SP-115, pp. 47–54.

KEVORKIAN, J. & COLE, J. D. 1981 *Perturbation Methods in Applied Mathematics.* Springer.

LANDOLT, J. P. & CORREIA, M. J. 1980 Neurodynamic response analysis of anterior semicircular canal afferents in the pigeon. *J. Neurophysiol.* **43**, 1746–1770.

LUTZ, R. J., LITT, M. & CHAKRIN, L. W. 1973 Physical-chemical factors in mucus rheology. In *J. Rheology of Biological Systems* (ed. H. L. Gabelnick & M. Litt), pp. 119–157. Charles C. Thomas, Springfield, IL.

MACH, E. 1875 *Grundlinien der Lehre von den Bewegungsempfindungen.* Leipzig: Wilhelm Engelman.

MCLAREN, J. W. & HILLMAN, D. E. 1979 Displacement of the semicircular cupula during sinusoidal rotation. *Neuroscience* **4**, 2001–2008.

OMAN, C. M., MARCUS, E. N. & CURTHOYS, I. S. 1987 The influence of semicircular canal morphology on endolymph flow dynamics. *Acta. Otolaryngol. (Stockh.)* **103**, 1–13.

PEDLEY, T. J., SCHROTER, R. C. & SUDLOW, M. F. 1971 Flow and pressure drop in systems of repeatedly branching tubes. *J. Fluid Mech.* **46**, 365–383.

RABBITT, R. D., BOYLE, R. & HIGHSTEIN, S. M. 1994 Sensory transduction of head velocity and acceleration in the toadfish horizontal semicircular canal. *J. Neurophysiol.* **72**, 1041–1048.

RABBITT, R. D., BOYLE, R. & HIGHSTEIN, S. M. 1995*a* Mechanical indentation of the vestibular labyrinth and the relationship to head rotation in the toadfish, *Opsanus tau. J. Neurophysiol.* **73**, 2237–2260.

RABBITT, R. D., BOYLE, R. & HIGHSTEIN, S. M. 1995*b* Simultaneous measurement of horizontal semicircular canal endolymph pressure and neural response in the toadfish, *Opsanus tau. Assoc. Res. Otolaryngol.* Feb. 7, St. Petersburg, FL.

RABBITT, R. D. & DAMIANO, E. R. 1992 A hydroelastic model of macromechanics in the endolymphatic vestibular canal. *J. Fluid Mech.* **238**, 337–369.

REDDY, J. N. 1984 *Energy and Variational Methods in Applied Mechanics.* John Wiley & Sons.

RÜSCH, A. & THURM, U. 1990 Spontaneous electrically induced movements of ampullary kinocilia and stereovilli. *Hearing Res.* **48**, 247–264.

SCHMID-SCHÖNBEIN, G. W., SUNG, K. L. P., TÖZEREN, H., CHIEN, S. & SKALAK, R. 1981 Passive mechanical properties of human leukocytes. *Biophys. J.* **36**, 243–256.

SEGALÖNBEIN, B. N. & OUTERBRIDGE, J. S. 1982 Vestibular (semicircular canal) primary neurons in the bullfrog: nonlinearity of individual and population response to rotation. *J. Neurophysiol.* **47**, 545–562.

STEER, R. W., LI, Y. T., YOUNG, L. R. & MEIRY, J. L. 1967 Physical properties of the labyrinthine fluids and quantification of the phenomenon of caloric stimulation. *Third Symp. on the Role of Vestibular Organs in Space Exploration.* NASA SP-152, pp. 409–420.

STEINHAUSEN, W. 1933 Über die beobachtungen der cupula in den bognegängsampullen des labyrinthes des libenden hecths. *Pflügers Arch. Ges. Physiol.* **232**, 500–512.

SUTERA, S. P., MUELLER, E. R. & ZAHALAK G. I. 1990 Extensional recovery of an intact erythrocyte from a tank-treading motion. *ASME J. Biomech. Engng* **112**, 250–256.

VAN BUSKIRK, W. C. 1987 Vestibular mechanics. In *Handbook of Bioengineering* (ed. R. Skalak & S. Chien), pp. 31.1–31.17. McGraw Hill.

VAN BUSKIRK, W. C. & GRANT, J. W. 1973 Biomechanics of the semicircular canals. *Biomechanics Symp. ASME, NY*, pp. 53–54.

VAN BUSKIRK, W. C., WATTS, R. G. & LIU, Y. K. 1976 The fluid mechanics of the semicircular canals. *J. Fluid Mech.* **78**, 87–98.

VAN DYKE, M. 1975 *Perturbation Methods in Fluid Mechanics.* The Parabolic Press.

WERSÄLL, J. & BAGGER-SJÖBÄCK, G. M. 1974 Morphology of the vestibular sense organ. In *Handbook of Sensory Physiology V6(1), Vestibular System Part I: Basic Mechanisms* (ed. H. H. Kornhuber), pp. 123–170. Springer.

WOMERSLEY, J. R. 1955 Method for the calculation of velocity, rate of flow, and viscous drag in arteries when the pressure gradient is known. *J. Physiol.* **127**, 553–563.

WOMERSLEY, J. R. 1958 Oscillatory flow in arteries I. The constrained elastic tube as a model of arterial flow and pulse transmission. *Phys. Med. Biol.* **2**, 177–187.